

Extinction Curves, Distances, and Clumpiness of Diffuse Interstellar Dust Clouds¹

Arpad Szomoru
and

Puragra Guhathakurta²
UCO/Lick Observatory, University of California, Santa Cruz, California 95064, USA

ABSTRACT

We present CCD photometry in *UBVRI* of several thousand Galactic field stars in four large (> 1 degree²) regions centered on diffuse interstellar dust clouds, commonly referred to as “cirrus” clouds (with optical depth A_V less than unity). Our goal in studying these stars is to investigate the properties of the cirrus clouds. A comparison of the observed stellar surface density between on-cloud and off-cloud regions as a function of apparent magnitude in each of the five bands effectively yields a measure of the extinction through each cloud. For two of the cirrus clouds, this method is used to derive *UBVRI* star counts-based extinction curves, and *U*-band counts are used to place constraints on the cloud distance. The color distribution of stars and their location in $(U - B, B - V)$ and $(B - V, V - I)$ color-color space are analyzed in order to determine the amount of selective extinction (reddening) caused by the cirrus. The color excesses, $A_\lambda - A_V$, derived from stellar color histogram offsets for the four clouds, are better fit by a reddening law that rises steeply towards short wavelengths [$R_V \equiv A_V/E(B - V) \lesssim 2$] than by the standard law ($R_V = 3.1$). This may be indicative of a higher-than-average abundance of small dust grains relative to larger grains in diffuse cirrus clouds. The shape of the counts-based effective extinction curve and a comparison of different estimates of the dust optical depth (extinction optical depth derived from background star counts/colors; emission optical depth derived from far infrared measurements), are used to measure the degree of clumpiness in clouds. The set of techniques explored in this paper can be readily adapted to the Sloan Digital Sky Survey data set in order to carry out a systematic, large-scale study of cirrus clouds.

Subject headings: ISM: clouds—dust, extinction—ISM: general—ISM: structure—stars: fundamental parameters—methods: statistical

¹Observations carried out at the Cerro Tololo Interamerican Observatory, National Optical Astronomy Observatories, which is operated by the Association of Universities for Research in Astronomy, Inc. under cooperative agreement with the National Science Foundation.

²Alfred P. Sloan Research Fellow

1. Introduction

Among the most remarkable of the many discoveries made by the *Infrared Astronomical Satellite* (*IRAS*, Neugebauer et al. 1984) was the detection of a bright component of the far infrared background emission. This far infrared component is marked by discrete condensations of filamentary clouds with characteristic sizes ranging between a few and $\sim 30^\circ$. Their resemblance to clouds in our own atmosphere led Low et al. (1984) to dub them the infrared “cirrus”. The cirrus clouds are most readily observed at high Galactic latitudes where there is relatively little contribution to the net background by the Galactic plane, and are most prominent at $100\,\mu\text{m}$, although they are visible in all four *IRAS* bands. Low et al. noted the positional correlation of some of the cirrus emission with HI clouds mapped by Heiles (1975) and interpreted this as evidence that the infrared cirrus was in fact associated with the diffuse interstellar medium (ISM).

Despite the fact that optical cirrus was first discovered over four decades ago (de Vaucouleurs 1955, 1960), definite association with high latitude dust came much later (de Vaucouleurs & Freeman 1972; Sandage 1976). The first systematic comparison between the *IRAS* $100\,\mu\text{m}$ and optical morphologies of dust clouds was conducted by de Vries & Le Poole (1985). This and a few other studies (Paley 1990; Stark 1993), all based on photographic data, reveal a good correspondence between optical and infrared cirrus. Quantitative optical surface brightness measurements of cirrus clouds have been carried out by Guhathakurta & Tyson (1989), Paley et al. (1991), and Gordon, Witt, & Friedmann (1998), while spectroscopy of diffuse cirrus clouds has been carried out only recently (Szomoru & Guhathakurta 1998). Such optical measurements provide important clues towards understanding grain optical properties, such as the albedo and the phase function asymmetry, and have demonstrated the existence of extended red emission, caused by photoluminescence in very small grains, in the diffuse ISM (Szomoru & Guhathakurta 1998; Gordon et al. 1998).

Diffuse cirrus clouds typically extend over large areas on the sky. Such clouds can be probed through the study of their effect on the light of background sources (Galactic stars, distant quasars). A statistical method which is well suited for cirrus clouds employs star counts to determine the extinction. This method,

which was first described and applied several decades ago (Wolf 1923; Bok 1937), has been used to determine the extinction in high latitude molecular clouds (cf. Magnani & de Vries 1986; Stark 1995). By comparing cumulative star counts in the direction of an interstellar cloud with star counts in extinction-free regions, or alternatively with model-based star counts (so-called Wolf diagrams—Wolf 1923), one may derive both the amount of extinction through and the distance to the cloud. An alternate method relies on optical and ultraviolet spectroscopy of individual background hot stars of known spectral type (Stark 1995) or QSOs with mostly featureless, power-law spectra (cf. Bowen 1991; Bowen, Blades, & Pettini 1995). This latter method is useful for the study of dust extinction curves, cloud chemical abundances, and excitation conditions in the gaseous ISM. It has been applied mostly to dense molecular clouds cores with $A_V \gg 1$ and to the warm ionized ISM of the Galaxy, rather than to cirrus clouds.

This paper presents photometry in *UBVRI* of several thousand stars in four large area ($> 1\text{ degree}^2$) fields centered on cirrus clouds. The surface photometry of these clouds will be the subject of a future paper. Our study differs from previous studies in several respects:

- CCD photometry of faint stars over a wide field is less subject to systematic error than photographic measurements thanks in large part to accurate flat fielding and sky subtraction.
- The use of *UBVRI* bands opens up the possibility of studying the effect of selective extinction by interstellar dust on stellar color distributions and color-color diagrams, in addition to its effect on star counts. This combination of techniques can be used to investigate the occurrence of dense cores and to quantify the amount of structure within the clouds (Sec. 6.2).
- Measurements of the effect of extinction on star counts/color distribution are made relative to a well-matched off-cirrus sample of stars, and this yields a reliable and precise determination of the extinction curve (A_λ).
- Data at short wavelengths (3600\AA *U* band) enables us to study clouds of relatively low optical depth; all four clouds studied here have A_V values significantly less than unity. Most previous

studies employing background star counts have been of molecular clouds with higher optical extinction than the cirrus clouds in our sample, with the study by Stark (1995) being a notable exception; in fact, two of our four clouds are also in his sample. In contrast to our *UBVRI* CCD data, however, the optical part of his study is based solely on *U*-band photographic plates.

Direct measurements of the optical extinction have a number of important applications. Firstly, the ratio of A_V (visual extinction optical depth) to $\tau_{100\mu\text{m}}$ (the far infrared emission optical depth) provides a test, albeit a crude one, of interstellar dust grain models. Such tests are now possible thanks to accurate A_V measurements, along with recent improvements in techniques for the processing of far infrared data and hence in the measurement of $\tau_{100\mu\text{m}}$ (Schlegel, Finkbeiner, & Davis 1998, hereafter SFD; Verter & Rickard 1998; Verter et al. 1998). Secondly, a direct measurement of A_V (as opposed to an approximate scaling based on the far infrared surface brightness) is essential in order to model the degree of penetration and internal reddening of ambient starlight in cirrus clouds; this is a key piece of information used in the interpretation of ultraviolet/optical/near-infrared spectra and *UBVRI* surface brightness measurements of optical cirrus.

The observations and reduction of optical data are described in Sec. 2 and far infrared measurements are described in Sec. 3. Sec. 4 contains the background star count analysis along with the resulting determination of the extinction law and cloud distance; Sec. 5 contains a description of stellar color-color diagrams and their use in the measurement of selective extinction (reddening). In Sec. 6, the optical extinction is compared to the $100\mu\text{m}$ optical depth, and optical depth estimates from the various methods are discussed in the context of cloud structure (i.e., clumpiness) and dust properties. Sec. 7 contains a summary of the main results.

2. Optical Data

2.1. Targets and Observations

Over the last decade, several compact, relatively isolated, high latitude cirrus clouds have been observed at optical wavelengths for the purpose of studying the reprocessing of starlight by interstellar dust grains (cf. Guhathakurta & Cutri 1994). These cirrus

targets have been selected from *IRAS* $100\mu\text{m}$ maps or drawn from optical cirrus catalogs such as the list of Lynds Bright Nebulae (Lynds 1965) or the compilation of Paley (1990) which are, in turn, derived from Palomar Observatory Sky Survey plates. This paper is based on observations of four such cirrus clouds, RCrA (R Corona Australis), PV 1 (Project Verification #1, an early-phase target of the Infrared Space Observatory), Paley 1, and Paley 3 (from the Paley 1990 catalog).

The observations were carried out with the Cerro Tololo Interamerican Observatory³ Curtis-Schmidt telescope, equipped with a Tektronix 2048×2048 CCD camera, during three nights in 1995 October. This telescope has a 0.9-m primary mirror and a 0.6-m corrector. The pixel size of $21\mu\text{m}$, corresponding to a scale of $2''.03 \text{ pixel}^{-1}$, yields a field of view of $1.15^\circ \times 1.15^\circ$. The finite filter size causes slight vignetting ($\sim 20\%$ at the extreme corners of each CCD frame) but this is well corrected by sky flat fields.

The Schmidt CCD observations consist of a series of disregistered 400 s exposures in the standard *UBVRI* filter set at Cerro Tololo Interamerican Observatory. The effective wavelengths of these filters are practically identical to those of the corresponding Johnson bandpasses: 3597\AA , 4405\AA , 5495\AA , 6993\AA , and 9009\AA , respectively. The total integration time for RCrA, PV 1, and Paley 3 is about 20–30 min per field in each of the *BVRI* bands, and about 50 min in the *U* band where the instrumental efficiency is very low. The integration times for the Paley 1 field are about a factor of 2 longer than in the corresponding bands for other three fields. For photometric calibration purposes, the Landolt Selected Area SA 92 (Landolt 1992) containing several standard stars was observed in *UBVRI* twice during the first night. Short twilight flat exposures in all five bands were obtained at the beginning and end of each night; several series of bias frames were obtained during the daytime. The FWHM of the stellar images ranges from $5''.1$ – $5''.7$ (2.5 – 2.8 pixels), the result of atmospheric seeing, imperfect focus, and coarse pixel scale. The coordinates and observational parameters of the clouds are listed in Table 1.

³Cerro Tololo Interamerican Observatory, National Optical Astronomy Observatories, is operated by the Association of Universities for Research in Astronomy, Inc. under cooperative agreement with the National Science Foundation.

TABLE 1
CLOUD COORDINATES AND OBSERVATIONAL PARAMETERS

(1)	(2)	(3)	(4)	(5)	(6)	(7)	(8)	(9)	(10)
Name	α_{2000} (^h ^m ^s)	δ_{2000} ([°] ['] ^{''})	l ([°])	b ([°])	$t_{\text{int}}(U)$ (min)	$t_{\text{int}}(B)$ (min)	$t_{\text{int}}(V)$ (min)	$t_{\text{int}}(R)$ (min)	$t_{\text{int}}(I)$ (min)
RCrA	18 56 04.1	−37 18 05	359.2	−16.9	47	27	20	20	27
PV 1	22 06 28.4	−03 32 33	56.5	−44.1	53	27	20	20	27
Paley 1	02 38 24.6	−29 43 36	225.6	−66.4	93	53	47	40	47
Paley 3	23 48 53.8	−71 47 12	309.7	−44.5	53	33	20	20	33

NOTE.—
Col. 6 – 10: Total integration time in minutes in each of the U , B , V , R , and I bands.

2.2. Data Reduction

As a first step, all the images (object, photometric calibration, and flat-field exposures) are overscan- and bias-subtracted and trimmed. The twilight flats and selected disregistered (dark sky) object exposures of all four cirrus clouds are combined into a master flat-field image for each of the $UBVRI$ bands; the master flat-field image is applied to all object and photometric calibration exposures. After flat fielding, image defects (e.g., hot pixels, charge traps, and bad columns) are replaced by the median value of the pixels surrounding the defects.

A set of relatively bright and isolated stars are selected in each of the four cirrus fields, and these are used to determine the linear shift in (x, y) between each of the images and a particular astrometric reference image. After registering the images approximately, the IRAF routine GEOMAP is applied to these same bright stars in order to determine higher order coordinate transformations (translation, rotation, magnification, distortion) for every image with respect to the reference image; the IRAF routine GEOTRAN is then used to accurately align all the images using the coordinate transformations determined by GEOMAP.

The median background sky level for each object exposure is subtracted from the image. The registered, sky-subtracted images of a given cirrus cloud

in a given band are then combined into a median-averaged image. In the case of the PV 1 field, the translational offsets between various exposures are quite large (of the order of the field of view of an individual CCD image); the final combined image in each band for PV 1 is the union of all the images in that band. As a result, the effective exposure time, and hence the r.m.s. sky noise level, varies with position across the final image of the PV 1 field. For the other three cirrus fields, only the intersection area of all exposures is used, and the noisy (partial overlap) edges of the combined images are discarded.

The final, combined V -band images of the four cirrus cloud fields are shown in Figure 1. The images contain several very bright, saturated stars with extensive and complicated charge bleed patterns; the exact number of saturated stars in the image depends on the Galactic latitude of the field (most numerous in RCrA) and on wavelength (many more in R - and I -band images than in UBV). Instead of attempting to model (and subtract) the intensity distribution of saturated stars, the affected regions in their vicinity are eliminated from further consideration, since detection and photometry of faint stars is unreliable in these regions. This is done by finding the positions of stars for which the central pixel value is above the saturation limit ($\sim 60,000$ ADU or 1.26×10^5 electrons) and determining the number of saturated pixels at

the center of every saturated star. An empirical relation is then defined between the number of saturated pixels at the center of a stellar image and the size of the associated region to be eliminated; this relation is used to mask a circular area of appropriate radius around every saturated star.

2.3. Stellar Photometry

Lists of object positions are generated independently for each of the five bands and for each of the four cirrus fields using the peak finding algorithm FIND of the stellar photometry program DAOPHOT (Stetson 1987, 1992). An object detection threshold of 3.5σ is used, where σ is the sky noise; in the case of the PV 1 field, the variation of sky noise level across the image (due to non-uniform effective exposure time) is taken into account.

Most of the detected objects are Galactic stars; a small fraction are distant field galaxies. Even at high Galactic latitudes ($|b| \gtrsim 30^\circ$), the surface density of stars exceeds that of field galaxies for $V \lesssim 20$ (cf. Kron 1980), roughly the apparent magnitude limit of our study (see Sec. 2.4 and Figs. 2 and 3). Given the relatively coarse angular resolution of our CCD data and the fact that the majority of the galaxies in the sample are expected to be close to the detection/completeness limit, no attempt has been made to exclude galaxies using morphological star-galaxy separation. In fact, field galaxies are just as useful as distant stars for studying the optical depth of a foreground cirrus cloud. In the rest of this paper, we loosely use the term “stars” to refer to the sample of detected (mostly stellar) objects.

An iterative procedure, based on a combination of several DAOPHOT tasks, is applied to the DAOPHOT/FIND star list in order to build an empirical point spread function template and to fit the template to every star in the list. Aperture photometry is carried out for each star in turn, with the results of the point spread function fit used to subtract off the light of the neighbors of the star in question. This combination of point spread function fitting and aperture photometry techniques is ideal for photometry of undersampled stellar images in crowded fields (Guha-thakurta et al. 1996). The aperture magnitudes, calculated over small (2 pixel radius) apertures to avoid neighbor contamination, are corrected to total magnitudes using standard “curve-of-growth” corrections. The curve of growth is determined independently for each band and for each cirrus field, based on the in-

tensity profiles of a set of isolated bright stars. The lists of star positions and corresponding total instrumental magnitudes are then combined into a position-matched *UBVRI* list for each cirrus field. Total instrumental magnitudes are also determined for photometric standard stars in the SA 92 calibration field using a similar curve-of-growth method.

As the SA 92 calibration field was only observed on the first (photometric) night, a bootstrap magnitude zeropoint adjustment is determined for each field and for each band: the airmass-corrected instrumental magnitudes of a sample of secondary standard stars in a single image obtained during that first night are compared to those measured on the median-averaged image. This zeropoint adjustment is quite small, ranging from 0.01 – 0.09 mag. One of the four fields (Paley 3) was not observed during the first night and thus could not be bootstrap corrected. However, the resulting error in the overall magnitude scale for this field is likely to be small (< 0.1 mag) and thus unimportant for the analysis in this paper.

The IRAF routine FITPARAM is used to derive the zeropoints and color- and airmass-coefficients of the transformation equations for converting instrumental magnitudes to calibrated Johnson-Kron-Cousins *UBVRI* magnitudes, based on measurements of the total instrumental magnitudes of photometric standard stars in the SA 92 field. The instrumental stellar magnitudes in the four cirrus fields are converted to calibrated *UBVRI* magnitudes using the routine INVERTFIT, adopting an airmass term that is the average of all the individual exposures for that band in each field. The transformation equations from $(UBVRI)_{\text{inst}} \rightarrow (UBVRI)_{\text{calib}}$ contain color terms based on $U - B$, $B - V$, $B - V$, $V - R$, and $R - I$, respectively. The corresponding color term coefficients are -0.034 , $+0.165$, -0.073 , $+0.027$, and -0.013 . Not all stars are detected in all bands; the combination of *BVI* detections is of particular interest to us (see Sec. 5.2), including a small subset of stars which happen to be undetected in the *R* band. To estimate the color term in the $I_{\text{inst}} \rightarrow I_{\text{calib}}$ relation for these *R*-band non-detections, their calibrated $R - I$ color is estimated using the empirical correlation between $(B - V)_{\text{calib}}$ and $(R - I)_{\text{calib}}$ that is seen for stars detected in all bands. This technique is accurate enough for our purposes since the *I*-band color term coefficient is very small.

For the star count analysis described in Sec. 4, star lists are also constructed on the basis of detec-

tions in a single band (e.g., U band only, B band only, etc.). These single-band detections are calibrated using an *average* color term in the instrumental \rightarrow Johnson conversion relation; for example: $U_{\text{calib}} = U_{\text{inst}} + \langle U_{\text{calib}} - U_{\text{inst}} \rangle$, where the average is computed over all stars for which a proper transformation is possible. Thus the calibrated $UBVRI$ magnitudes in the single band lists are only approximations to true calibrated magnitudes with proper color terms. This approximation however should be quite good as the color term coefficients are generally small.

2.4. Completeness

The completeness of the single-band star lists as function of magnitude, $N_{\text{obs}}/N_{\text{true}}$, is modeled as a double exponential:

$$N_{\text{obs}}/N_{\text{true}} = 0.5 [2 - \exp(-(m - m_{50})/\Delta m)] \quad (1)$$

$$m \leq m_{50}$$

$$N_{\text{obs}}/N_{\text{true}} = 0.5 [\exp(-(m - m_{50})/\Delta m)] \quad (2)$$

$$m > m_{50}$$

The underlying star count versus apparent magnitude relation, N_{true} , is assumed to be a power law in the vicinity of the 50% completeness point, m_{50} . The values of the two free parameters m_{50} and Δm (sharpness with which incompleteness sets in) are then determined by fitting to the shape of the observed count distribution, N_{obs} . At magnitudes brighter than the completeness limit, the observed counts are a good fit to the Bahcall-Soneira model (Bahcall & Soneira 1980; see Sec. 4.3 and Fig. 2), which predicts N_{true} to be roughly a power law over the magnitude range of interest. The typical value of Δm is about 0.4, with a range from 0.3 to 0.6, while the 50% completeness values range from $I_{50} \approx 18$ to $U_{50} \approx 21$ (as indicated in Figs. 2 and 3).

3. Far Infrared Data

The *IRAS* 100 μm (ISSA) maps provided by the Infrared Processing and Analysis Center are used to divide each optical image into three regions on the basis of 100 μm surface brightness, $F_{100\mu\text{m}}$. The mean brightness, $\langle F_{100\mu\text{m}} \rangle_{\text{bg}}$, and pixel-to-pixel r.m.s. variation, $\sigma_{100\mu\text{m}}$, of the 100 μm background is computed

in regions without visible optical cirrus. An “off-cirrus” region is defined in which

$$F_{100\mu\text{m}} < \langle F_{100\mu\text{m}} \rangle_{\text{bg}} + 5\sigma_{100\mu\text{m}},$$

along with two “on-cirrus” regions:

$$\langle F_{100\mu\text{m}} \rangle_{\text{bg}} + 5\sigma_{100\mu\text{m}} < F_{100\mu\text{m}} < \langle F_{100\mu\text{m}} \rangle_{\text{bg}} + 11\sigma_{100\mu\text{m}} \text{ (“on1”)}$$

and

$$F_{100\mu\text{m}} > \langle F_{100\mu\text{m}} \rangle_{\text{bg}} + 11\sigma_{100\mu\text{m}} \text{ (“on2”).}$$

Each star in the matched $UBVRI$ list and single-band lists is then flagged according to the region in which it falls. The background 100 μm flux, r.m.s. variation, and the areas of the “off”, “on1”, and “on2” regions for each cirrus field are listed in Table 2. These areas are indicated on the V -band images of the four clouds shown in Figure 1.

As discussed in Sec. 6 below, the optical depth of a cirrus cloud can be estimated both from its effect on the counts/colors of background stars (extinction optical depth) and from its far infrared brightness and color temperature (emission optical depth). The far infrared emission-based estimate is derived from full sky 100 μm maps provided by SFD. These maps are a reprocessed composite of the *COsmic Background Explorer/Diffuse InfraRed Background Experiment* (*COBE/DIRBE*) and *IRAS* (ISSA) maps, with zodiacal foreground and confirmed point sources removed. The procedure combines the relatively high angular resolution of *IRAS* 100 μm data ($3'$) with the superior photometric calibration of *DIRBE* data, and is estimated to be twice as accurate as the older Burstein & Heiles (1982) reddening maps in regions of low to moderate reddening. In addition to 100 μm flux maps with improved photometric calibration, SFD compute $F_{100\mu\text{m}}^{\text{corr}}$ over the full sky, the equivalent 100 μm flux corrected for variations in mean dust temperature from one line of sight to another. The amount of reddening, $E(B - V)$, is calculated by normalizing the amplitude of reddening per unit of corrected 100 μm flux, based on the observed reddening towards brightest cluster galaxies and elliptical galaxies. The $E(B - V)$ values of SFD are scaled by $R_V \equiv A_V/E(B - V) = 3.1$ to derive differential on-cloud A_V values (“on1”–“off”, “on2”–“off”) for each of the four cirrus clouds in this study (Table 3 and Fig. 13).

SFD present all-sky maps of the dust temperature, averaged along the line of sight, derived from the ratio of *DIRBE* 100 μm to 240 μm flux measurements. The effective angular resolution of the temperature measurements is limited to $\sim 1^\circ$ by the resolution of

the *DIRBE* far infrared data. The mean dust temperature of each of the four cirrus clouds in this study (averaged over “on1” and “on2” regions) is listed in Table 2. The implications of cloud-to-cloud variations in dust temperature will be discussed in Sec. 6.3.

SFD assume a standard extinction law with $R_V = 3.1$ in deriving $E(B - V)$ values which should be correct on average over the full sky. The lines of sight towards the four clouds in this study, however, may have R_V values that are different from this standard value (see Sec. 4.2 and 5.1). For a line of sight with a non-standard extinction law, the SFD value of $E(B - V)$ will be inaccurate, but the estimate of A_V should be valid. SFD’s estimate is effectively based on $\tau_{100\mu\text{m}}$ (correcting the $100\mu\text{m}$ flux to the average dust temperature). The variation in extinction law from one line of sight to another appears to be mostly in terms of the relative amount of extinction at wavelengths at or shortwards of the B band while the portion redward of the V band is invariant in shape (Cardelli, Clayton, & Mathis 1989, hereafter CCM; Martin & Whittet 1990). In other words, our estimate of A_V is valid under the assumption that extinction laws along different lines of sight, normalized by $\tau_{100\mu\text{m}}$, are similar for $\lambda \gtrsim \lambda_V$ and diverge only at shorter wavelengths.

4. Star Counts

4.1. Analysis of Cumulative Star Counts

Single-band star lists are used to derive star counts in each band and for each region (“off”, “on1”, and “on2”) of each field. The single-band star lists are preferable to the matched *UBVRI* lists for this purpose, as they are based on clean, well-defined selection functions and contain more stars by virtue of a higher degree of completeness at the faint end. Figure 2 shows cumulative star counts versus apparent magnitude, also called Wolf diagrams (Wolf 1923), for the four cirrus fields in the U band; Figure 3 shows Wolf diagrams for RCrA in *BVRI*. As these diagrams are based on single-band detections, the photometric conversion to the Johnson magnitude system is only approximate (Sec. 2). The “on1” and “on2” distributions shown in Figures 2 and 3 have been normalized to match the area of the “off” region distributions. Areas around bright saturated stars (where the detection and photometry of faint stars is unreliable) are excluded from the analysis. Table 2 lists the usable area of the V -band image, properly ac-

counting for the masked (excluded) regions around saturated stars. These masked regions are slightly different in the different bands for a given cirrus field; since saturation tends to be most severe at the longest wavelengths, the R - and I -band images have typically smaller usable areas than the U -band images. The saturated stars themselves are included in the star count analysis by adding the number of saturated stars in each field and each band to the bright end of the cumulative distributions. The total star count ranges from $\sim 24,000$ in U to $\sim 51,000$ in V for RCrA, and from $\sim 2,000$ in U to $\sim 7,000$ in V for Paley 1, the fields with the highest and lowest star densities, respectively, in our sample.

A typical cumulative star count relation roughly resembles a power law, but has slight curvature such that the slope, $S_\lambda \equiv d \log[N(< m_\lambda)]/dm_\lambda$, gets shallower towards fainter apparent magnitudes (Figs. 2 and 3). The relations are uncertain at the bright end due to the small number of stars; the abrupt flattening at the faint end marks the onset of incompleteness. There is a range of slopes from field to field and a characteristic trend in S_λ versus *UBVRI*, with the slopes steepening towards both shorter and longer wavelengths relative to the V band. This is likely the result of two competing effects. On the one hand, intrinsically faint (lower main sequence) stars tend to have redder colors than intrinsically luminous stars (turnoff/upper main sequence), causing the I -band slope to be steeper than the V -band slope. On the other hand, the “depth” of the sample, in terms of the typical distance of stars at the magnitude limit in each band, decreases from V towards U . The U -band slope is close to the Euclidean value of 0.6 expected for a constant star density, while the mean distance of the V -band sample is large enough for the fall-off in Galactic star density along the line of sight to be noticeable. The star count slope is relevant to the discussion of the effects of clumpiness (Sec. 6.2).

It is evident from Figures 2 and 3 that dust extinction in the intervening cirrus cloud causes each on-cloud star count relation to be shifted towards fainter magnitudes (i.e., to the right) with respect to the corresponding off-cloud relation. The magnitude of these shifts decreases from U to I as expected on the basis of the normal interstellar dust extinction law. Moreover, the shift between the “on2” (the region with highest $100\mu\text{m}$ flux) and “off” star count curves is consistently larger than the shift between “on1” and “off” curves across the *UBVRI* bands, at least in the

TABLE 2
PROPERTIES OF CIRRUS CLOUDS

(1) Name	(2) $\langle F_{100\mu\text{m}} \rangle_{\text{bg}}$ (MJy sr $^{-1}$)	(3) $\sigma_{100\mu\text{m}}$ (MJy sr $^{-1}$)	(4) Area $_{\text{off}}$ (deg 2)	(5) Area $_{\text{on1}}$ (deg 2)	(6) Area $_{\text{on2}}$ (deg 2)	(7) T_{on} (K)
RCrA	9.3	0.6	0.61	0.21	0.15	17.8
PV 1	5.6	0.3	0.85	0.43	0.49	17.5
Paley 1	0.19	0.05	0.47	0.09	0.32	17.7
Paley 3	1.0	0.1	0.83	0.18	0.16	18.0

NOTE.—

Col. 2: Mean background 100 μm flux in regions without visible cirrus.

Col. 3: Pixel-to-pixel r.m.s. variation in background 100 μm flux.

Col. 4–6: Area of “off”, “on1”, and “on2” regions (V -band), which refer to regions with fluxes that are $< 5\sigma$, 5σ – 11σ , and $> 11\sigma$ above the 100 μm background. Note, these areas are slightly different across $UBVRI$ because of differences in the area lost to saturated stars.

Col. 7: Mean dust temperature in on-cloud region from *DIRBE* far infrared measurements (Schlegel et al. 1998).

two fields (RCrA and PV1) for which the shifts are measured reliably for both “on2” and “on1” regions.

4.2. Star Counts-Based Extinction Curves

The magnitude shift between Wolf diagrams on and off an obscuring cloud is a direct measure of the effective dust extinction, $A_{\lambda}^{\text{counts}}$, at least at faint apparent magnitudes where the contribution of low luminosity foreground stars is unimportant and the on and off curves run parallel to each other. As explained in Sec. 6.2 below, the $A_{\lambda}^{\text{counts}}$ value derived from the magnitude shift in a Wolf diagram yields a measure of the effective “extinction” that depends on the degree of clumpiness of the dust distribution (even for a given mean dust optical depth and a given set of grain optical properties).

Wolf diagram shifts are plotted in Figure 4 as a function of apparent magnitude in the *UBVRI* bands for all four cirrus cloud fields. The median value of $A_{\lambda}^{\text{counts}}$ is computed over an intermediate range of apparent magnitudes, avoiding excessive Poisson noise at the bright end and the divergence of the Wolf diagram shift at the faint end caused by the flattening of the cumulative star counts due to incompleteness. In the cases of the “on1” and “on2” regions of the RCrA and PV1 fields, the Wolf diagram shifts are sufficiently large for the extinction to be measurable in all five bands. For Paley 1 and Paley 3 on the other hand, the extinction is lower and the measurement errors larger (see discussion of errors below) so that a reliable measurement is only possible at the shortest wavelengths and that too for only the “on2” regions (*U* band for Paley 1, *U* and *B* bands for Paley 3); for these two fields the A_U and A_B values are scaled to A_V assuming a specific form of the extinction law, either a standard law with $R_V = 3.1$ or an $R_V = 1.7$ law (CCM).

Figure 5 provides an illustration of the typical errors in the determination of the Wolf diagram apparent magnitude shift $A_{\lambda}^{\text{counts}}$. The errors in $A_{\lambda}^{\text{counts}}$ are derived from the statistical uncertainties in the star counts, projected onto the magnitude axis (abscissa) using the slope of the $\log[N(< m_{\lambda})]$ -vs- m_{λ} relation (roughly a power law over the apparent magnitude range of interest), combined with the photometric uncertainties. The errors are of the order of 0.2 – 0.3 mag for RCrA, the field with the largest number of stars. Poisson error dominates throughout most of the plotted apparent magnitude range; the contribution of the photometric error becomes noticeable

beyond $V \sim 17 - 18$ in RCrA (somewhat fainter in Paley 3). Increasing photometric error, in conjunction with the flattening of the cumulative star count relations, causes the flaring of the $A_{\lambda}^{\text{counts}}$ error bands at the faint end.

The effective extinction curves for the “on1” and “on2” regions of RCrA and PV1 derived from star counts are shown as open squares and triangles, respectively, in Figure 6. The $A_{\lambda}^{\text{counts}}$ estimates are uncertain for the Paley 1 and Paley 3 fields (all but the “on2” estimates at the shortest wavelengths) so extinction curves are not presented for these two clouds. The lines are analytic approximations to the extinction law provided by CCM for different R_V values. The RCrA and PV1 extinction curves are reasonable approximations to the standard extinction law with $R_V = 3.1$ (solid line).

Looking more closely, the PV1 “on2” extinction curve rises more steeply towards short wavelengths (*U* band) than the standard extinction law, suggesting a lower value of R_V . A minimum of the χ^2 statistic is obtained for $R_V = 1.7$ (dashed line). For RCrA on the other hand, the increase of $A_{\lambda}^{\text{counts}}$ with decreasing wavelength is somewhat more gradual than for the standard extinction curve, with A_I^{counts} being particularly discrepant. While this would appear to favor high R_V values in that the χ^2 statistic decreases with increasing R_V , there is no clear χ^2 minimum over the plausible range of parameter space ($R_V < 7$). Alternatively, a good fit to the RCrA $A_{\lambda}^{\text{counts}}$ measurements is obtained by assuming a non-uniform dust density (dotted line; Sec. 6.2) with $R_V = 3.1$ or even with $R_V = 1.7$, the lower R_V value being preferable in light of the color excess data for this cloud (see Sec. 5.1). We will return to a discussion of the counts-based extinction curves in Sec. 6.2.

The weighted average of the $A_{\lambda}^{\text{counts}}$ measurements in *UBVRI* is computed for RCrA and PV1, after the measurement in each band is scaled to the equivalent A_V estimate using the analytic form of the extinction law for a specific R_V (Table 3 and Fig. 13). While the choice of R_V affects the quality of the fit to the five $A_{\lambda}^{\text{counts}}$ measurements, the weighted average A_V^{counts} is practically independent of R_V , and tends to be similar to the measured value of $A_{\lambda}^{\text{counts}}$ in the *V* band. In other words, changing R_V results in a steep or shallow extinction curve, but the best-fit curves intersect near the middle of the range of available data points which happens to be the *V* band.

4.3. Star Count Models

Wolf diagrams have traditionally been used to determine both the extinction through and the distance to dust clouds. Distance determination, in particular, requires knowledge of the stellar luminosity function and the spatial density distribution of stars along the line of sight. Based on this information, theoretical Wolf diagrams can be constructed for various values of the dust extinction and distance of an obscuring cloud. These diagrams can then be directly compared to the star count data.

Theoretical Wolf diagrams are generated for the four cirrus clouds in this study using the IASG Galaxy Model program (Bahcall, Casertano, & Ratnatunga 1987; Ratnatunga, Bahcall, & Casertano 1989; Casertano, Ratnatunga, & Bahcall 1989), which is based on the Bahcall-Soneira star count model of the Galaxy (Bahcall & Soneira 1980; Bahcall 1986). The IASG program yields the total projected density of stars and their distribution as a function of apparent V magnitude, $B - V$ color, and distance modulus, for any specified direction. A Monte-Carlo realization of these distributions is carried out in order to construct a stellar sample. Next, $U - B$ colors are computed using the Bertelli et al. (1994) stellar evolution models, averaging over all available ages per metallicity, for four different metallicities, $Z = 0.0004$, $Z = 0.008$, $Z = 0.05$ and $Z = 0.02$. The product is a list of stars with UBV magnitudes and distance moduli for each metallicity from which cumulative star counts are computed appropriate for the off-cloud region. The dust cloud is assumed to be (geometrically) thin; it produces an apparent offset of A_λ for all stars located at distances greater than that assigned to the dust cloud. The resulting list is used to construct on-cloud model star count relations. As the model results are similar for the four different metallicities, only curves computed with $Z = 0.05$ are shown.

The slopes of the model cumulative star count relations, plotted as dotted blue lines in Figures 2 and 3, agree well with the observed slopes, with the possible exception of PV1. An offset has been applied to the apparent magnitude scale in the Bahcall-Soneira model in order to match the observed counts in the “off” region: $+0.2$, $+1.5$, -0.2 , and -0.5 mag for RCrA, PV1, Paley3 and Paley1, respectively. Positive corrections to the apparent magnitude may indicate that the overall extinction integrated over the line of sight is not quite zero even in the off-cloud re-

gions. There may, however, also be small systematic errors in the model (e.g., in the apparent magnitude scale, or in the normalization of the stellar density or luminosity function) that cause it to deviate from the observed counts. Note that since the curves (model and observed counts) are good approximations to single power laws, a horizontal shift is roughly equivalent to a vertical shift [in the $\log(N)$ direction].

4.4. Cloud Distance Determination

Model on-cloud and off-cloud Wolf diagrams are constructed for the RCrA and PV1 fields using IASG star count predictions coupled with a geometrically thin dust slab located at various line-of-sight distances. These model curves are shown as dotted blue lines in the upper panel of Figures 2 and 3 for a cloud distance of 550 pc and an optical depth of $A_U = 0.9$ (matching the “on2” measurements of A_U^{counts} in the two clouds), which scales to $A_V = 0.6$ on the basis of a standard extinction law. The on-cloud model curves for RCrA shown in the center and bottom panels of Figure 7 are for cloud distances of 400 pc and 800 pc, respectively, for optical depths of $A_U = 0.9$ (“on2”; left) and $A_U = 0.3$ (“on1”; right).

Only RCrA and PV1, the fields with the lowest latitude and largest area, respectively, contain enough bright stars ($U \sim 13 - 15$; see discussion below) and high enough extinction for us to obtain reliable constraints on the distance using this method. Figure 7 compares the RCrA “on2” and “on1” Wolf diagrams (upper left and upper right panels, respectively) with their corresponding IASG model-based Wolf diagrams for cloud distances of $d = 0.4$ kpc (center panel) and $d = 0.8$ kpc (bottom panel), bracketing the likely distance of the RCrA cloud. The best estimate of the RCrA cloud distance is in the range 550 – 750 pc. For PV1, it is only possible to place an upper limit to the distance of about 1 kpc. The distance determination is uncertain for PV1 due to its low stellar surface density: the Poisson error in this field is 40% larger than in RCrA despite its $3.3\times$ larger area.

The IASG model Wolf diagrams shown in the center and bottom panels of Figure 7 are based on a very large number of synthetic stars in order to minimize the effect of Poisson error. A realistic measure of the dispersion in cumulative star count relations is obtained by making several Monte Carlo realizations of the on-cloud model, with each realization containing the number of stars appropriate for the actual area

of the RCrA on-cloud (“on2” or “on1”) region being simulated. The dispersion among the realizations of a given model can be used to judge the significance with which the model fits or is ruled out by the data; the $\pm 1\sigma$ error bars in the center left panel of Fig. 7 indicate the dispersion for the RCrA “on2” $d = 0.4$ kpc model. Averaging over the $U = 12 - 15$ mag range, 66% of the $d = 0.4$ kpc model realizations lie below the RCrA “on2” star count curve, while 82% of the $d = 0.8$ kpc model realizations lie above it (both models adopt $A_U = 0.9$). Comparing the $A_U = 0.3$ model to the RCrA “on1” star count curve, 54% of the $d = 0.4$ kpc realizations lie below the data while 90% of the $d = 0.8$ kpc realizations lie above the data.

The differences between the on-cloud and off-cloud model cumulative star count curves can be understood in simple terms. The transition between majority-foreground and majority-background in the on-cloud star count relation occurs at an apparent magnitude equal to that of a “typical” star at the distance of the cloud. While stars have a wide range of absolute magnitudes, the characteristic absolute magnitude is defined by an abrupt rise near the bright end of the stellar luminosity function. The rise is at the main sequence turnoff, $M_V^{\text{MSTO}} \approx +3.5$, for any old stellar population, and is particularly steep in the U band ($M_U^{\text{MSTO}} \approx +4.0$). Thus a cirrus cloud at a distance of 0.4 kpc (0.8 kpc), corresponding to a distance modulus of $(m - M)_0 = 8.0$ mag (9.5 mag), is expected to have a transition region at $U \sim 12.0$ ($U \sim 13.5$), in agreement with the model curves shown in the center (bottom) panel of Figure 7.

5. Effect of Reddening on Stellar Colors

In this section, the distribution of stellar colors is compared between on- and off-cloud regions for the purpose of exploring the reddening (selective extinction) caused by dust. In contrast to the star count analysis described in the previous section, the color analysis described in this section makes no use of the number or number density of stars in the various regions, and only uses information about the normalized stellar color distribution in each region (“off”, “on1”, and “on2”). As discussed in Sec. 6 below, star counts and color distributions provide complementary measures of the optical depth of a cirrus cloud.

5.1. Cumulative Color Distributions and Color Excess Measurements

A direct way to determine the amount of reddening caused by the cirrus cloud is to measure the difference in the stellar colors between on- and off-cloud regions. This is done by constructing normalized cumulative color histograms in $U - V$, $B - V$, $R - V$, and $I - V$ for the “off”, “on1”, and “on2” regions of the cirrus cloud fields. The median horizontal (i.e., color) difference between on-cloud and off-cloud histograms is defined to be the color excess, $E(m_\lambda - V) \equiv A_\lambda - A_V$, for $\lambda = UBRI$. Sample cumulative $U - V$ and $I - V$ color histograms are displayed in Figure 8 (solid and dashed lines, respectively) for the “on2” and “off” regions (thin and bold lines, respectively) of RCrA (upper panel) and Paley 3 (lower panel), with the horizontal line segment indicating the median value of the offset in each case. The color excess is well determined for most fields and colors, with the exception of long wavelength measurements for the low optical depth clouds, Paley 1 and Paley 3 [as illustrated by the Paley 3 $E(I - V)$ data in Fig. 8].

If a small fraction of the area of the “on1” or “on2” region of the cloud happens to have a much larger optical depth than the rest, it is effectively ignored by the use of the median in the color offset computation; the significance of this aspect of our measurement technique is discussed further in Sec. 6.2. The median offset is also insensitive to dilution by unreddened, bright, foreground stars, especially as these are greatly outnumbered by background stars.

The median color excess, $E(m_\lambda - V)$ for $m_\lambda = UBRI$, for the “on1” and “on2” regions of the four cirrus clouds is plotted as open squares and triangles in Figure 9. The dashed and solid lines show the CCM analytic approximation for the Galactic interstellar reddening law for $R_V = 3.1$ for “on1” and “on2”, respectively, while the dotted line shows an $R_V = 1.7$ reddening law for “on2”. Each analytic curve is scaled by the appropriate weighted mean value of the visual optical depth, A_V^{excess} , derived from the four color excess measurements (listed in Table 3 and shown in Fig. 13). As expected, A_V^{excess} is sensitive to the choice of R_V ; this is in contrast to the A_V^{counts} estimate derived from the $A_\lambda^{\text{counts}}$ measurements (Sec. 4.2).

The measured color excesses tend to increase more steeply with increasing $1/\lambda$ ($V \rightarrow U$) than the best-fit standard $R_V = 3.1$ reddening law, and vary less strongly with λ from $V \rightarrow I$ than the standard red-

dening law. In all cases, the $R_V = 1.7$ reddening law shown in Figure 9 appears to be a better match to the shape of the observed $E(m_\lambda - V)$ versus $1/\lambda$ than the standard reddening law. Applying a χ^2 test to the RCrA and PV 1 color excess data, a minimum of the χ^2 statistic, albeit a relatively shallow one, is found for R_V values that are substantially lower than the standard Galactic value of 3.1. The Paley 1 and Paley 3 χ^2 behavior also favors a low value of R_V ($\lesssim 2$) but there is no clear minimum as the Poisson error in these fields is larger than for RCrA or PV 1.

Note, the χ^2 test is only used in a relative way here. The χ^2 values are *not* used to decide if the CCM analytic form of the reddening law with a specific value of R_V is a good fit to the data in an absolute sense; the exact value of χ^2_{\min} is not particularly meaningful because: (1) the $E(m_\lambda - V)$ error estimates used in the χ^2 test are only approximate representations of the true (likely non-Gaussian) error distribution; and (2) the R_V -parametrized analytic formula used in the analysis is known to deviate from the measured reddening law in certain lines of sight (Cardelli & Clayton 1991).

5.2. Color-Color Diagrams

A second way to determine the cloud optical depth is through the use of color-color diagrams. This method is similar in principle to the color excess method described above except that a pair of stellar colors [e.g., the $(U - B, B - V)$ pair or the $(B - V, V - I)$ pair] is analyzed jointly. As the intrinsic spread in stellar $V - R$ and $R - I$ colors is not very broad relative to the photometric errors in these quantities, the R -band data are excluded from this analysis and the longer $V - I$ color baseline is used instead for a more accurate measurement of the reddening.

Figure 10 shows the $U - B$ versus $B - V$ and $V - I$ versus $B - V$ color-color diagrams (upper and lower panels, respectively) for RCrA and PV 1 (left and right panels, respectively). The Paley 1 and Paley 3 fields contain too few stars and the reddening in these clouds is too low for an analysis of their color-color distributions. The black, red, and green points indicate stars in the “off”, “on1”, and “on2” regions, respectively, plotted in this order. The blue lines show theoretical loci, computed from the Bertelli et al. (1994) stellar evolution models by averaging all available ages per metallicity, for three metallicities: $Z = 0.0004$, $Z = 0.008$, and $Z = 0.05$ (top

to bottom). The large spread of points is due to a combination of photometric errors, intrinsic range of stellar colors (spread in metallicity and age), sample contamination by background galaxies, spurious detections/matches, etc..

The arrows in Figure 10 indicate reddening vectors (CCM) corresponding to $A_V = 2$ mag for a standard extinction law with $R_V = 3.1$ (red) and for an $R_V = 1.7$ extinction law (black). The latter extinction law is a reasonable approximation to the available star count and color excess data for the four clouds. The progressive shift along the reddening vector of the “on1” and “on2” stellar color-color distributions with respect to the “off” distribution is clearly visible in RCrA, and is somewhat less obvious in PV 1. The principal direction along which the stellar distribution is extended is almost parallel to the reddening vector, especially in the $V - I$ vs $B - V$ plot; even so, an accurate statistical measurement of the reddening is rendered possible by the use of a well-matched off-cloud region and the large numbers of stars in the sample (which enables accurate determination of the centroid of the stellar distribution).

The amount of reddening in the color-color diagrams is estimated by measuring the shifts between on- and off-cloud stellar distributions projected onto the direction of the reddening vector. The sample of stars is divided into a series of contiguous slices parallel to the reddening vector each of width 0.1 mag. The median offset along the length of the slice is computed between the “on1”/“on2” and “off” distributions for each slice. The final visual optical depth estimate is a weighted average of the median shifts derived from the different slices. These optical depth estimates are denoted A_V^{UBV} and A_V^{BVI} for the $(U - B, B - V)$ and $(V - I, B - V)$ plots, respectively. The offsets (in A_V units) for the individual slices of the RCrA $U - B$ vs $B - V$ diagram are illustrated in Figure 11 for “on2” (solid line) and “on1” (dashed line). The error bars indicate the combined standard error in the mean centroids of the on- and off-cloud stellar distributions. The weighted mean of the individual slice offsets is indicated by the horizontal dot-dashed line.

A test is carried out in order to assess the effect of incompleteness at the faint end of the sample, or, more specifically, the effect of differential incompleteness between on- and off-cloud samples which may introduce a bias in the color offset measurement. The “off” sample is artificially reddened by an arbitrary amount corresponding to an optical depth of

A_V^{sim} . This simulated reddened sample is then folded through the completeness function in the three bands of interest (i.e., UBV or BVI). The offset of the on-cloud sample is measured with respect to the simulated reddened and truncated sample. The process is iterated while varying A_V^{sim} until there is a null offset between simulated and on-cloud samples. The value of A_V^{sim} that produces a null offset is found to be virtually identical to the directly measured value of the visual optical depth (A_V^{UBV} or A_V^{BVI}), so it may be concluded that differential incompleteness effects are unimportant in the determination of A_V from color-color diagrams.

The calculation of A_V^{UBV} and A_V^{BVI} for the “on1” and “on2” regions of RCrA and PV 1 is done two ways, assuming a standard $R_V = 3.1$ reddening law or the steeper $R_V = 1.7$ reddening law. The resulting A_V estimates are listed in Table 3 and shown in Figure 13. The second set of A_V values are understandably lower than the first: a lower R_V produces a steeper extinction law in the blue portion of the spectrum (i.e., stronger variation with λ), so that a fixed (observed) color offset corresponds to a smaller A_V . A secondary effect is that the directions of the $R_V = 3.1$ and $R_V = 1.7$ reddening vectors are slightly different in the $(V - I, B - V)$ plane and this leads to different projections of the stellar color-color offsets.

In contrast to the star count and color excess analysis described above (Sec. 4.2 and 5.1), a specific form of the reddening law had to be assumed *a priori* in deriving A_V from color-color diagrams. Given the similar orientations of the $R_V = 3.1$ and $R_V = 1.7$ reddening vectors (directions almost degenerate in $U - B$ vs $B - V$ plot), it is impossible to determine *both* R_V and A_V independently from a single color-color diagram, even for a field containing as many stars as RCrA. It would require a very large, uncontaminated sample of stars and accurate photometry to exploit the subtle dependence of reddening vector direction on R_V in the $(V - I, B - V)$ plane. Alternatively, the combination of all four available colors can discriminate between different R_V values (cf. Sec. 5.1).

6. Discussion

6.1. Reddening Law in Diffuse Cirrus Clouds

Studies of the interstellar extinction law along various lines of sight in the Galaxy show some evidence for a dependence of R_V on environment. Dense regions such as optically thick molecular clouds, of which

the ρ Oph dark cloud is a typical example (Martin & Whittet 1990), tend to have relatively shallow extinction curves indicating R_V values larger than the global average of 3.1, while regions of low density display extinction curves that rise steeply towards short wavelengths indicating lower-than-average R_V values (cf. Mathis 1990), although some counter examples do exist. The fact that all four diffuse clouds in our sample have reddening laws that favor lower R_V values is in keeping with this trend. Also consistent with the findings of this paper is the observed steepening of the far-ultraviolet extinction curve with increasing distance from the Galactic plane (Kiszkurno-Koziej & Lequeux 1987). On the face of it, the RCrA data appear to yield conflicting results: a higher-than-average R_V value fits the star counts-based extinction curve (Sec. 4) while a lower-than-average value fits the color excess measurements. As explained in Sec. 4.2 and 6.2, however, all of the RCrA data are adequately explained by $R_V \lesssim 2$ if one invokes a non-uniform dust density.

The R_V values for the four cirrus clouds in this study are unusually low, although comparable values have been observed in a few instances. A study of about 200 OB stars by Whittet & van Breda (1980) found a minimum value of $R_V = 2.4$, while the subsequent survey by Fitzpatrick & Massa (1990) found a minimum value of $R_V = 2.6$ for the line of sight towards HD 204827. More recently, Larson, Whittet, & Gough (1996) reported a value of $R_V = 2.1$ for the high-latitude cloud DBB 80 based on their study of the early type star HD 210121.

The observed variations in the shape of the interstellar extinction law from one line of sight to another are predominantly at blue and ultraviolet wavelengths while the red and infrared portion remains invariant (Martin & Whittet 1990). Variations in R_V , the ratio of selective blue-minus-visual extinction to total extinction, are generally thought to be a result of variations in the size distribution of dust grains: the total visual optical depth is determined by the abundance of large grains, while the extinction in the blue and ultraviolet portion is dominated by smaller grains (cf. CCM; Larson et al. 1996). Thus, a steep extinction curve is caused by a higher than average proportion of small size particles in a dust cloud. An abundance of small particles may be explained in terms of the cirrus being in a UV-poor and weak radiation environment in which grain destruction by photon heating is inefficient. An alternative explanation is that

the growth, by coagulation, of larger size particles is inhibited by the low overall density of the cloud (Larson et al. 1996).

6.2. Effect of a Clumpy Medium

In this section, we investigate the effect of a clumpy cirrus cloud on the counts and colors of background stars. The technique of using normalized color histograms to measure the reddening caused by cirrus (Sec. 5) yields the average optical depth for the lines of sight towards the specific set of stars used in the color analysis. If there is substantial non-uniformity in the dust column density within a given cloud region (“on1” or “on2”), so much so that a highly-reddened subset of background stars drops out of the matched *UBVRI* sample, the color-based method will underestimate the true area-weighted average optical depth. Wolf diagrams, on the other hand, are sensitive (in a statistical sense) to stars that have dropped out of the on-cloud sample (Sec. 4). In addition to the “horizontal” shift to fainter apparent magnitudes of the on-cloud cumulative star count curve due to extinction of stars in the sample, any highly-attenuated undetected subset of stars will cause a “vertical” downward shift in the curve, which is equivalent to a shift to the right since the star count relation closely resembles a power law.

The characterization of a clumpy medium is, in general, complicated and beyond the scope of this paper. Instead, the essential features of a non-uniform dust cloud are illustrated with the help of a simple two-phase model: a fractional area f of the absorbing material is assumed to have a uniform and relatively low optical depth of A_V^{sheet} while the remaining fraction $(1 - f)$ is covered by dense clumps with optical depth A_V^{clump} . Exact calculations are carried out for the particular case: $A_V^{\text{clump}} \rightarrow \infty$. Since the Wolf diagram shift is statistical in nature, the following calculations involve no assumptions about the morphology of the low and high extinction regions. However, considering that a large contiguous area with $A_V \rightarrow \infty$ would be conspicuous in the CCD images, a low extinction sheet with numerous small dense clumps seems a more likely scenario.

With the above assumptions, and given the specifics of the measurement method used (Sec. 5), the color excess histograms and color-color diagrams measure the extinction in the smooth, low optical depth part of the cloud, A_λ^{sheet} . The Wolf diagram shift is greater

than A_λ^{sheet} but its exact value depends on the shape of the cumulative star count function. For the purposes of this calculation, the off-cloud number count relation is assumed to be a power law with slope S_λ : $N_{\text{off}}(< m_\lambda) = C_\lambda 10^{S_\lambda m_\lambda}$, where C_λ is a normalization constant. The cumulative star count function in the on-cloud (“on1” or “on2”) region is then a power law with the same slope: $N_{\text{on}}(< m_\lambda) = C_\lambda \left[f 10^{S_\lambda(m_\lambda - A_\lambda^{\text{sheet}})} + (1 - f) 10^{S_\lambda(m_\lambda - A_\lambda^{\text{clump}})} \right]$. Thus, the Wolf diagram shift, $(A_\lambda^{\text{counts}})_{\text{model}}$, is directly proportional to the “vertical” shift between the on- and off-cloud relations at a fixed apparent magnitude m_λ .

$$(A_\lambda^{\text{counts}})_{\text{model}} = \frac{1}{S_\lambda} [\log(N_{\text{off}}) - \log(N_{\text{on}})] \quad (3)$$

$$= \frac{-1}{S_\lambda} \log \left[f 10^{-S_\lambda A_\lambda^{\text{sheet}}} + (1 - f) 10^{-S_\lambda A_\lambda^{\text{clump}}} \right] \quad (4)$$

Under the assumption that $A_\lambda^{\text{clump}} \gg 1$ over the wavelength range of interest, this simplifies to:

$$(A_\lambda^{\text{counts}})_{\text{model}} = \frac{-\log(f)}{S_\lambda} + A_\lambda^{\text{sheet}} \quad (5)$$

where the first term accounts for the undetected fraction of background stars while the second term is the extinction caused by the smooth sheet on the rest of the stars. The *V*-band version of the above equation may be rewritten as:

$$\log(f) = S_V \left[A_V^{\text{sheet}} - (A_V^{\text{counts}})_{\text{model}} \right] \quad (6)$$

Normalizing the counts-based “effective” extinction (Eq. 5) by the *V*-band value and substituting for f using Eq. 6, it follows that:

$$\left[\frac{A_\lambda^{\text{counts}}}{A_V^{\text{counts}}} \right]_{\text{model}} = \frac{S_V}{S_\lambda} + \left[r_\lambda - \frac{S_V}{S_\lambda} \right] \frac{A_V^{\text{sheet}}}{(A_V^{\text{counts}})_{\text{model}}} \quad (7)$$

where $r_\lambda \equiv (A_\lambda/A_V)$ depends only on the shape of the extinction law. The *UBVRI* star count slopes vary somewhat from field to field (see Sec. 4.1 for a discussion of the general trends in S_λ).

A one-parameter family of normalized counts-based “effective” extinction curves, computed by varying the ratio $A_V^{\text{sheet}}/(A_V^{\text{counts}})_{\text{model}}$ for a standard $R_V = 3.1$ extinction law (CCM) and using the observed

star count slopes S_λ in the RCrA field, is shown in Figure 12. An increasing degree of non-uniformity (decreasing f) results in a flattening of the counts-based extinction curve. The effect of clumpiness is qualitatively similar for other extinction laws as well (e.g., $R_V = 1.7$). Although Eq. 7 depends only on the ratio $A_V^{\text{sheet}}/A_V^{\text{counts}}$ and not on the value of A_V^{counts} itself, the derived value of the area covering fraction f does depend on A_V^{counts} (Eq. 6). Moreover, the normalized counts-based extinction curves display a similar behavior with increasing clumpiness even if the $A_V^{\text{clump}} \rightarrow \infty$ assumption is relaxed, although their exact shapes in that case depend somewhat on the value of A_V^{counts} .

There is an apparent discrepancy in the case of RCrA. The Wolf diagram shifts for this cloud, $A_\lambda^{\text{counts}}$, increase less steeply with decreasing wavelength than the standard $R_V = 3.1$ extinction law, indicating a larger R_V value (Sec. 4.2). On the other hand, the color excesses for the same cloud are a steep function of wavelength and are adequately described by the $R_V = 1.7$ CCM reddening law (Sec. 5.1). This discrepancy can be resolved if the dust column density in RCrA is non-uniform. For example, the $A_\lambda^{\text{counts}}$ measurements can be fit by a combination of $R_V = 1.7$ and a smooth sheet fraction of $f = 0.8$, which corresponds to $A_V^{\text{sheet}}/A_V^{\text{counts}} = 0.5$ and $A_V^{\text{sheet}} = 0.3$ (this translates to $f = 0.7$ for $A_V^{\text{counts}} = 1$ in Fig. 12). The combinations ($R_V = 3.1$, $f = 0.9$) and ($R_V \sim 5$, $f = 1$) produce $A_\lambda^{\text{counts}}$ vs λ functions that are practically identical in shape to the ($R_V = 1.7$, $f = 0.8$) case and they all fit the RCrA measurements equally well (see dotted line in Fig. 6). Considering the low R_V value implied by the RCrA color excess data, the first solution seems the most plausible, in spite of the degeneracy of the fits to the $A_\lambda^{\text{counts}}$ data.

6.3. Comparing Different Measures of the Dust Optical Depth

The preceding sections outline a variety of methods used to measure the dust extinction optical depth of a few representative diffuse interstellar cirrus clouds: empirical scaling of the $100\mu\text{m}$ flux after correction for temperature variations (Sec. 3), analysis of the background star count density as a function of apparent magnitude (Sec. 4), reddening of stellar color distributions (Sec. 5.1), and shifts of the stellar color-color distribution (Sec. 5.2). The different methods measure slightly different quantities (as quantified in Sec. 6.2). Nevertheless, the methods yield general

consistency for a given cloud. The full set of A_V estimates, based on both the standard $R_V = 3.1$ value and the preferred $R_V = 1.7$ value, are listed in Table 3 and plotted in Figure 13.

The agreement between different A_V estimates for the PV 1 cloud is especially good if one adopts $R_V \lesssim 2$ in deriving A_V from the color excess and color-color data (filled symbols in the second panel of Fig. 13)—the observed trends of $A_\lambda^{\text{counts}}$ and $E(m_\lambda - V)$ versus λ for this cloud are, in any case, indicative of a low R_V . The RCrA “on2” region A_V estimates, particularly those based on $R_V = 1.7$ (filled triangles in panel 1 of Fig. 13), display the largest discrepancy: A_V^{counts} is twice as large as estimates based on the color excess and color-color distribution and is significantly smaller than the $100\mu\text{m}$ flux-based estimate, $A_V^{100\mu\text{m}}$. As discussed in Sec. 6.2 above, this is best explained in the context of the simple two-phase model of a clumpy cirrus medium. The dotted line in panel 1 of Figure 13 indicates a model designed to match the RCrA “on2” observations: $R_V = 1.7$, $f = 0.8$, $A_V^{\text{sheet}} = 0.3$, and $A_V^{\text{counts}} = 0.6$. The estimates based on color excess and color-color data, A_V^{excess} , A_V^{UBV} , and A_V^{BVI} , correspond to A_V^{sheet} . The counts-based estimate, A_V^{counts} , is boosted by the presence of high density clumps. The far infrared flux-based estimate, $A_V^{100\mu\text{m}}$, is expected to be larger than both the color- and counts-based estimates and is nominally a weighted average of A_V^{sheet} and A_V^{clump} . However, since the characteristic size of the dense clumps is likely to be smaller than the coarse ($\sim 1^\circ$) angular resolution of the far infrared data and since the dust in the dense clumps is likely to be colder than the dust in the low density sheet (because of self-shielding), the flux-weighted average temperature derived by SFD is likely to be biased in favor of the temperature of the warmer dust in the sheet. The A_V estimate derived from the scaling of $F_{100\mu\text{m}}^{\text{corr}}$ (Sec. 3) is then lower than the “true” area-weighted average optical depth. The lower and upper branches of the dotted line in panel 1 of Figure 13 show the area-weighted average A_V for $A_V^{\text{clump}} = 2.4$ and 3.5 , respectively; these bracket the measured $A_V^{100\mu\text{m}}$ for RCrA “on2”. The actual optical depth of the dense clumps could be significantly higher, so it is plausible that stars behind such clumps drop out of the matched *UBVRI* sample—this is equivalent to setting $A_V^{\text{clump}} \rightarrow \infty$ in the Wolf diagram analysis (Sec. 6.2).

The ratio of visual optical depth to far infrared brightness, $A_V/F_{100\mu\text{m}}$, is in the range 0.06–0.08 for

TABLE 3
EXTINCTION ESTIMATES

(1) Name	(2) R_V	(3) Region	(4) $A_V^{100\mu\text{m}}$	(5) A_V^{counts}	(6) A_V^{excess}	(7) A_V^{UBV}	(8) A_V^{BVI}
RCrA	3.1	on1	0.25 ± 0.02	$0.26 \pm 0.04^{\text{a}}$	0.10 ± 0.02	0.18 ± 0.01	0.05 ± 0.01
	3.1	on2	0.77 ± 0.04	$0.61 \pm 0.04^{\text{a}}$	0.46 ± 0.04	0.45 ± 0.01	0.36 ± 0.01
	1.7	on1		$0.26 \pm 0.03^{\text{a}}$	0.07 ± 0.01	0.11 ± 0.01	0.06 ± 0.01
	1.7	on2		$0.61 \pm 0.04^{\text{a}}$	0.27 ± 0.02	0.26 ± 0.01	0.25 ± 0.01
PV 1	3.1	on1	0.16 ± 0.01	0.24 ± 0.06	0.33 ± 0.18	0.36 ± 0.04	0.28 ± 0.04
	3.1	on2	0.35 ± 0.01	0.46 ± 0.07	0.65 ± 0.18	0.55 ± 0.03	0.52 ± 0.04
	1.7	on1		0.21 ± 0.06	0.20 ± 0.11	0.16 ± 0.02	0.13 ± 0.03
	1.7	on2		0.42 ± 0.06	0.37 ± 0.10	0.31 ± 0.02	0.32 ± 0.02
Paley 1	3.1	on1	0.05 ± 0.01		0.16 ± 0.06		
	3.1	on2	0.16 ± 0.01	$0.12 \pm 0.23^{\text{b}}$	0.24 ± 0.07		
	1.7	on1			0.11 ± 0.04		
	1.7	on2		$0.09 \pm 0.17^{\text{b}}$	0.16 ± 0.04		
Paley 3	3.1	on1	0.06 ± 0.01		0.08 ± 0.08		
	3.1	on2	0.14 ± 0.01	$0.13 \pm 0.11^{\text{b}}$	0.17 ± 0.08		
	1.7	on1			0.06 ± 0.05		
	1.7	on2		$0.09 \pm 0.09^{\text{b}}$	0.10 ± 0.04		

^a A_V^{counts} is determined by fitting the $UBVRI$ Wolf diagram shifts to a clumpy cirrus cloud model: standard $R_V = 3.1$ extinction law with a fraction $(1 - f) = 0.1$ of the cloud area covered by optically thick dense clumps, or with $R_V = 1.7$ and $(1 - f) = 0.2$ (Sec. 6.2).

^b A_V^{counts} is scaled, using the standard $R_V = 3.1$ extinction law or $R_V = 1.7$, from A_U^{counts} in the Paley 1 “on2” region or from A_U^{counts} and A_B^{counts} in the Paley 3 “on2” region. The rest of the “on2” and all “on1” $A_\lambda^{\text{counts}}$ values are poorly constrained.

NOTE.—

Col. 4: Derived from $100\mu\text{m}$ flux (Sec. 3).
Col. 5: Derived from $UBVRI$ star counts/Wolf diagrams (Sec. 4).
Col. 6: Derived from $UBVRI$ color excesses (Sec. 5.1).
Col. 7: Derived from UBV color-color diagram (Sec. 5.2).
Col. 8: Derived from BVI color-color diagram (Sec. 5.2).

RCrA (“on1” and “on2”), Paley 1 (“on2”), and Paley 3 (“on2”), and in the range 0.12–0.13 for PV 1 (“on1” and “on2”). These results are in good agreement with other measurements of diffuse interstellar clouds: 0.05–0.1 in Stark’s (1995) study of isolated, high-latitude clouds (including Paley 1 and Paley 3); 0.05 in an all-sky survey by Boulanger & Péroult (1988); and 0.04 in a cirrus cloud in the direction of the Polaris star (Zagury et al. 1999).

The $F_{100\mu\text{m}}$ values quoted above for the cirrus clouds in this study are the calibrated far infrared fluxes from SFD, *uncorrected* for dust temperature. Using the temperature-corrected flux, $F_{100\mu\text{m}}^{\text{corr}}$ (the flux a cloud would have if it were at the global average dust temperature of $\langle T \rangle = 18.0$ K), lowers the $A_V/F_{100\mu\text{m}}^{\text{corr}}$ ratio to 0.04–0.06 for RCrA, Paley 1, and Paley 3, and to 0.07–0.09 for PV 1. These clouds are colder than the typical dust cloud in the Galaxy (see Table 2), probably due to the absence of strong heating sources. Thus, the temperature correction causes $F_{100\mu\text{m}}^{\text{corr}}$ to be greater than $F_{100\mu\text{m}}$, and the $A_V/F_{100\mu\text{m}}^{\text{corr}}$ to be correspondingly lower. The typical large dust cloud complex in the Boulanger & Péroult (1988) study is in a hotter radiation environment than the cirrus clouds in our sample and the Zagury et al. (1999) cloud is thought to be heated in part by the Polaris star; this may explain why their $A_V/F_{100\mu\text{m}}$ measurements are at the low end of the range found in this study. If the SFD temperature estimates are taken literally, the observed difference between $A_V/F_{100\mu\text{m}}$ for PV 1 versus the other clouds is not due to cloud-to-cloud variations in dust temperature, but instead reflects variations in dust optical properties and/or measurement error.

6.4. Future Prospects: Sloan Digital Sky Survey Data

The techniques described in this paper are applied to four representative cirrus clouds. However, the application and the results derived from it are limited by several factors including: field of view of the observations (~ 1 deg²), photometric depth of the stellar sample ($V_{\text{lim}} \approx V_{50} \sim 20$), photometric accuracy (typically $\sigma \gtrsim 0.1$ mag), and the cirrus cloud sample size (4). In the case of very thin cirrus, a large number of background stars and accurate photometry are needed to make an accurate determination of the extinction. This can be accomplished by using a larger field of view and/or increasing the photometric depth. Determination of cloud distance can only be

achieved with a substantial number of (bright) foreground stars, and this requires a wide field of view. A large sample of optically thin cirrus clouds must be studied before the conclusions about low R_V , small grains, and clumpiness can be extrapolated to the general diffuse ISM.

The Sloan Digital Sky Survey (SDSS) data set should combine several of the desired properties outlined above. The SDSS is an ongoing digital photometric and spectroscopic survey covering 10^4 deg² in the North Galactic cap, and a deeper imaging survey in the South Galactic hemisphere covering 225 deg². Accurate photometry is being carried out in five bands, u' , g' , r' , i' , and z' (spanning the entire near-ultraviolet to optical range), complete to limiting point source magnitudes of $m_{\text{AB}} = 22.3, 23.3, 23.1, 22.3$, and 20.8 , respectively in the North Galactic cap. The southern portion of the survey should extend about 2 mag fainter than the northern portion. The entire photometric survey is expected to include over 10^8 stars and galaxies.

Application of the photometric methods explored in this paper to the SDSS database should yield a reliable and detailed extinction map, one that is based on direct measurement as opposed to scaling of far infrared flux, along with excellent statistics for the measurement of cloud distances. This exercise will likely go hand in hand with the development of a new empirical star count model of the Galaxy, a refinement of the Bahcall-Soneira model. The SDSS northern sample is expected to be about 2 mag deeper than the sample analyzed in this study, and this corresponds to about an order of magnitude increase in the surface density of background objects. The increased density of background tracers should translate to an increase in the angular “resolution” of the resulting extinction map, especially for the southern part of the SDSS survey. The SDSS opens up the prospect of obtaining a three-dimensional map of cirrus clouds over a quarter of the sky and conducting an extensive study of diffuse interstellar dust clouds.

7. Summary

We develop techniques for investigating the optical depth, constituent grain properties, structure, and distance of diffuse interstellar dust clouds. The study is based on *UBVRI* CCD photometry of several thousand stars in four $\gtrsim 1$ deg² fields centered on Galactic cirrus clouds from which well matched on- and off-

cloud samples are constructed. The main points of the paper are summarized below:

- A CCD-based variant of the 75-yr old Wolf diagram method is used to measure the effective extinction in different bands for the four cirrus clouds. Star counts-based *UBVRI* extinction curves are presented for two clouds, RCrA and PV 1. The steepness of the PV 1 extinction curve implies $R_V \equiv A_V/E(B-V) \lesssim 2$, which is unusually low compared to the standard Galactic value of $R_V = 3.1$.
- A comparison of normalized cumulative stellar color distributions on and off the cirrus cloud yields color excesses, $E(m_\lambda - V)$ for $m_\lambda = UBRI$. The reddening laws for all four cirrus clouds are steep, indicative of R_V values which are significantly lower than the standard value.
- The optical depth of the RCrA and PV 1 clouds is also determined from the shift of the stellar distribution in $U-B$ vs $B-V$ and $B-V$ vs $V-I$ color-color diagrams. This method depends on an assumed value of R_V which determines the length, and to a lesser extent, direction of the unit reddening vector. Sample incompleteness at the faint end is found to be unimportant for the color-color analysis.
- The four cirrus clouds in this study appear to favor unusually low values of R_V ($\lesssim 2$), comparable to the lowest values found in previous studies. This fits in with the clouds' low optical depth ($A_V < 1$) and the general trend of increasing R_V with increasing optical depth (and vice versa) that is observed for the interstellar medium of the Galaxy. The low R_V values in optically thin cirrus clouds is suggestive of a relative overabundance of small dust grains.
- Constraints on cloud distances are obtained by studying the cumulative star counts versus apparent magnitude relations on and off the cirrus in the context of the Bahcall-Soneira star count model of the Galaxy. The RCrA cloud is estimated to lie at a distance of 550–750 pc, while the distance to the PV 1 cloud is < 1 kpc.
- The effects of a non-uniform dust column density are illustrated through a simple two-phase model: a low extinction sheet with embedded

high density clumps. A clumpy medium tends to flatten (i.e., decrease the degree of wavelength dependence of) the star counts-based effective extinction curve. It also causes the counts-based A_V estimate to be higher than estimates based on color excess and color-color data and lower than the estimate based on far infrared flux. The RCrA Wolf diagram and stellar color data are readily explained in terms of a non-uniform medium in which 20% of the area is covered by dense clumps.

- Estimates of the dust optical depth derived from *UBVRI* extinction and reddening measurements are in good agreement with those based on the 100 μm flux. The values of the $A_V/F_{100\mu\text{m}}$ ratios for the four clouds are consistent with the ratios found in other studies of diffuse Galactic dust clouds and follow the expected trends in dust temperature.
- It should be possible to apply the photometric techniques described in this paper to the vast Sloan Digital Sky Survey data set in order to carry out an extensive study of dust properties in the diffuse interstellar medium and to construct an extinction map.

A.S. and P.G. are supported in part by NASA Long Term Space Astrophysics grant NAG 5-3232; PG is supported in part by an Alfred P. Sloan Foundation fellowship. We would like to thank Jean-Philippe Bernard for assistance with the observations.

REFERENCES

- Bahcall, J. N., & Soneira, R. M. 1980, *ApJS*, 44, 73
- Bahcall, J. N. 1986, *ARA&A*, 24, 577
- Bahcall, J. N., Casertano, S., & Ratnatunga, K. U. 1987, *ApJ*, 320, 515
- Bergbusch, P., & Vandenberg, D. A. 1992, *ApJS*, 81, 163
- Bertelli, G., Bressan, A., Chiosi, C., Fagotto, F., & Nasi, E. 1994, *A&AS*, 106, 275
- Bok, B. 1937, in *The Distribution of Stars in Space* (University of Chicago Press, Chicago)
- Boulanger, F., & Péroult, M. 1988, *ApJ*, 330, 964
- Bowen, D. V. 1991, *MNRAS*, 251, 649

- Bowen, D. V., Blades, C. J., & Pettini, M. 1995, *ApJ*, 448, 662
- Burstein, D., & Heiles, C. 1982, *ApJS*, 54, 33
- Cardelli, J. A., & Clayton, G. C. 1991, *AJ*, 101, 1021
- Cardelli, J. A., Clayton, G. C., & Mathis, J. S. 1989, *ApJ*, 345, 245
- Casertano, S., Ratnatunga, K. U., & Bahcall, J. N. 1989, *ApJ*, 357, 435
- de Vaucouleurs, G. 1955, *Observatory*, 75, 129
- de Vaucouleurs, G. 1960, *Observatory*, 80, 106
- de Vaucouleurs, G., & Freeman, K. C. 1972, *Vistas Astron.*, 14, 163
- de Vries, C. P., & le Poole, R. S. 1985, *A&A*, 145, L7
- Fitzpatrick, E. L., & Massa, D. 1990, *ApJS*, 72, 163
- Gordon, K. D., Witt, A. N., & Friedmann, B. C. 1998, *ApJ*, 498, 522
- Guhathakurta, P., & Cutri, R. M. 1994, in *ASP Conf. Ser. 58, The First Symposium on the Infrared Circrus and Diffuse Interstellar Clouds*, ed. R. M. Cutri & W. B. Latter (San Francisco: ASP), 101
- Guhathakurta, P., & Tyson, J. A. 1989, *ApJ*, 346, 773
- Guhathakurta, P., Yanny, B., Schneider, D. P., & Bahcall, J. N. 1996, *AJ*, 111, 267
- Heiles, C. 1975, *A&AS*, 20, 32
- Kiszkurno-Koziej, E., & Lequeux, J. 1987, *A&A*, 185, 291
- Kron, R. G. 1980, *ApJS*, 43, 305
- Landolt, A. U. 1992, *AJ*, 104, 340
- Larson, K. A., Whittet, D. C. B., & Hough, J. H. 1996, *ApJ*, 472, 755
- Low, F. J. et al. 1984, *ApJ*, 278, L19
- Magnani, L., & de Vries, C. P. 1986, *A&A*, 168, 271
- Martin, P. G., & Whittet, D. C. B. 1990, *ApJ*, 357, 113
- Mathis, J. S. 1990, *ARA&A*, 28, 37 105, 373
- Neugebauer, G. et al. 1984, *ApJ*, 278, L1
- Paley, E. S. 1990, M.S. thesis, University of Arizona
- Paley, E. S., Low, F. J., McGraw, J. T., Cutri, R. M., & Rix, H.-W. 1991, *ApJ*, 376, 335
- Ratnatunga, K. U., Bahcall, J. N., & Casertano, S. 1989, *ApJ*, 339, 106
- Sandage, A. 1976, *AJ*, 81, 954
- Schlegel, D. J., Finkbeiner, D. P., & Davis, M. 1998, *ApJ*, 500, 525
- Stark, R. 1993, Ph.D. thesis, University of Leiden
- Stark, R. 1995, *A&A*, 301, 873
- Stetson, P.B. 1987, *PASP*, 99, 191
- Stetson, P. B. 1992, in *ASP Conf. Ser. 25, Astronomical Data Analysis Systems and Software I*, ed. D. M. Worrall, C. Biemesderfer, & J. V. Barnes (San Francisco: ASP), 297
- Szomoru, A., & Guhathakurta, P. 1998, *ApJ*, 494, L93
- Verter, F., & Rickard, L. J., III. 1998, *AJ*, 115, 745
- Verter, F., Magnani, L., Dwek, E., & Rickard, L. J., III. 1998, in preparation
- Whittet, D. C. B., & van Breda, I. G. 1980, *MNRAS*, 192, 467
- Wolf, M. 1923, *Astr. Nachr.*, 219, 109
- Zagury, F. et al. 1999, *A&A*, in preparation

Fig. 1.— Greyscale (negative) representation of the V-band CCD images of the four cirrus cloud fields. The bold white contours indicate the on-cloud (“on1” and “on2”) and off-cloud (“off”) regions, demarcated on the basis of $100\,\mu\text{m}$ brightness. North is up and east is to the left. The scale of each image is indicated; the PV 1 image covers $1.8\,\text{deg}^2$, while each of the other three images covers about $1\,\text{deg}^2$. The optical surface brightness enhancement visible in the on-cloud region (relative to the off-cloud region) is due to reprocessing (mostly scattering) of ambient starlight by interstellar dust grains. The RCrA field is at the lowest Galactic latitude of the four fields ($|b| = 17^\circ$) and consequently contains the highest surface density of Galactic field stars. Areas around bright, badly saturated stars are excluded from data analysis.

Fig. 2.— Cumulative star counts versus calibrated apparent U -band magnitude (Wolf diagrams) in the four cirrus cloud fields. The y -axis numbers refer to the observed counts in the “off” region (solid black line); the “on1” (solid green line) and “on2” (solid red line) counts have been normalized to match the area of the “off” region (the “on1” counts are not shown for Paley 1 and Paley 3). The total number of saturated stars in each field and in each band (for which photometry is unavailable) is added to the bright end of the cumulative distribution. As expected, the “on2” (region with highest $100\,\mu\text{m}$ brightness) shifts are larger than the “on1” shifts. The dotted blue lines indicate Bahcall-Soneira star count models for the “off” and “on2” regions (upper and lower curve, respectively; see Sec. 4.4 and Fig. 7) of RCrA and PV 1, and for the “off” region of Paley 1 and Paley 3. The overall shape of the observed cumulative star counts (roughly a power law, with slight curvature) agrees well with that of the model relations, except for the flattening due to sample incompleteness at the faint end. The apparent U magnitude at which the sample is 50% complete, U_{50} , is indicated by a vertical dashed line for each field.

Fig. 3.— Same as Figure 2 for the RCrA field in the $BVRI$ bands, with Bahcall-Soneira star count models shown only for the B and V bands. Note the general trend of decreasing shifts between on-cloud and off-cloud star count relations as one moves towards longer wavelengths ($m_\lambda = U \rightarrow I$).

Fig. 4.— The apparent magnitude shift between on- and off-cloud cumulative star counts, $A_\lambda^{\text{counts}}$, plotted

as a function of calibrated apparent magnitude m_λ in the $UBVRI$ bands (light blue, dark blue, green, red, and black lines, respectively) for the four cirrus clouds. The “on1” regions of Paley 1 and Paley 3 are not shown as the shifts are only marginally significant. As expected, the shifts decrease systematically with increasing wavelength from U to I for a given cloud/region and tend to be higher in “on2” than “on1”.

Fig. 5.— Estimate of the uncertainty in the $A_\lambda^{\text{counts}}$ values derived from star counts in the U and I bands (solid and dashed lines, respectively) for RCrA (field with highest star density) and Paley 3. The $\pm 1\sigma$ error band, plotted as a function of calibrated apparent magnitude m_λ (U or I), is derived from the statistical uncertainty in the star counts, projected onto the magnitude axis using the slope S_λ of the $\log[N(< m)]$ -vs- m relation, combined with the photometric uncertainty. Poisson error dominates through most of the plotted apparent magnitude range; photometric error and incompleteness cause the flaring of the error bands at the faint end.

Fig. 6.— Effective extinction curve for RCrA and PV 1 based on $A_\lambda^{\text{counts}}$, the median apparent magnitude (horizontal) offset between cumulative star counts in “off” versus “on1”/“on2” regions (squares and triangles, respectively, with 1σ error bars), plotted as a function of inverse wavelength. The $A_\lambda^{\text{counts}}$ measurements for the other two clouds, Paley 1 and Paley 3, are not accurate enough for the computation of an extinction curve. The solid line shows the fiducial extinction curve from Cardelli et al. (1989) scaled to the weighted average value of the visual optical depth A_V^{counts} (see Table 3) for the average Galactic value of $R_V \equiv A_V/E(B-V) = 3.1$. For the RCrA cirrus cloud, the fit is improved (relative to the uniform dust slab case, $f = 1$) if we assume that the interstellar medium is clumpy with $(1-f) = 0.1$ of the cloud area covered by optically thick dense clumps of dust (dotted line); an identical fit can be made assuming $R_V = 1.7$ and $(1-f) = 0.2$. For the PV 1 “on2” region, the fit is improved by adopting $R_V = 1.7$ (dashed line), which corresponds to the blue/ultraviolet portion of the dust extinction curve rising more steeply than for the standard extinction curve ($R_V = 3.1$).

Fig. 7.— Enlarged section of the U -band Wolf diagram for the RCrA cloud (upper panel) and several

realizations of the Bahcall-Soneira star count model (center and lower panels). The star counts in the “off”, “on2”, and “on1” regions are indicated by bold solid, dotted, and thin solid lines, respectively, for the observations as well as the models. The $U \sim 11 - 15$ mag range shown represents the transition region between bright apparent magnitudes, for which the bulk of the stars are in front of the cirrus, and faint apparent magnitudes, for which most of the stars are in the background. Star count models are computed with and without an intervening slab of absorbing material, at distances of 0.4 kpc and 0.8 kpc that span the range of possibilities (center and lower panels, respectively), and with extinction corresponding to the measured $A_V^{\text{counts}} = 0.89$ mag in “on2” (left panel) and $A_V^{\text{counts}} = 0.34$ mag in “on1” (right panel). The 1σ error bars in the center left panel are derived from an ensemble of model realizations each using the number of stars appropriate for the actual RCrA “on2” area.

Fig. 8.— Sample cumulative $U - V$ (solid) and $I - V$ (dashed) color distributions of stars in the “on2” (thin) and “off” (bold) regions of the RCrA and Pa-ley 3 fields. The horizontal bar indicates the median color excess shift measured in each case. An arbitrary offset (in magnitudes) has been applied to each $m_\lambda - V$ ($m_\lambda = U$ or I) color scale in each field for convenience in plotting.

Fig. 9.— Color excess, $E(m_\lambda - V) \equiv A_\lambda - A_V$ ($\lambda = UBRI$), derived from the median shift in the cumulative stellar color distribution (Fig. 8) of “on1” (squares) and “on2” (triangles) with respect to the “off” region, plotted as a function of inverse wavelength for the four cirrus fields. A standard $R_V = 3.1$ Cardelli et al. (1989) reddening law scaled to the weighted average value of the visual optical depth A_V^{excess} (see Table 3) is plotted for the “on1” (dashed line) and “on2” region (solid line). The dotted line shows the best-fit $R_V = 1.7$ curve for the “on2” region. Only the “on2” errorbars are shown for the sake of clarity.

Fig. 10.— Color-color diagrams, $U - B$ versus $B - V$ and $V - I$ versus $B - V$, for stars in the “off” (black), “on1” (green), and “on2” (red) regions of the RCrA and PV 1 fields (overplotted in this order). A shift between the on- and the off-cloud stellar distributions is visible, most clearly in the case of the RCrA UBV plot. Theoretical color-color loci from the Bertelli

et al. (1994) stellar evolution models are shown as solid blue lines, averaged over all available ages for three different metallicities: $Z = 0.0004$, $Z = 0.008$, and $Z = 0.05$ (top to bottom). Reddening vectors corresponding to $A_V = 2$ mag are plotted for the standard $R_V = 3.1$ extinction law (red arrow) and for $R_V = 1.7$ (black arrow). A given offset in the color-color plane translates to a *larger* A_V for a standard interstellar reddening law than for an $R_V = 1.7$ law.

Fig. 11.— Illustration of the shift of the on-cloud [“on1” (dashed) and “on2” (solid)] stellar UBV color-color distribution with respect to the off-cloud distribution, measured along the $R_V = 3.1$ reddening vector, for the RCrA field. The stellar distributions are compared in a series of 0.1 mag-wide slices parallel to the reddening vector, and Δ is the offset of each slice in the direction perpendicular to the reddening vector relative to an arbitrary origin. The median offset between “on2”/“on1” and “off” stellar distributions along each slice is plotted, along with 1σ error bars based on the width of the distribution and the number of stars. The dot-dashed horizontal line indicates the best-fit value of the visual optical depth, A_V^{UBV} , derived from the weighted mean of the offsets measured in the individual slices.

Fig. 12.— The effect of clumpiness on the shape of the counts-based extinction curve, plotted in the normalized form: $A_\lambda^{\text{counts}}/A_V^{\text{counts}}$ versus inverse wavelength. The calculation is based on a simple two-phase model for the cirrus cloud (see Sec. 6.2) comprised of a smooth sheet of absorbing material with optical depth A_V^{sheet} and dense, opaque clumps ($A_V^{\text{clump}} \rightarrow \infty$). A one-parameter family of model counts-based extinction curves is obtained by varying the ratio, $A_V^{\text{sheet}}/A_V^{\text{counts}}$, for a fixed value of $A_V^{\text{counts}} = 1$, the overall offset in the V -band Wolf diagram. The curves shown are computed using the star count slopes S_λ measured in the RCrA field and a standard $R_V = 3.1$ extinction law. The quantity f is area covering factor of the low-optical depth, “sheet” portion of the cloud, and the listed values are based on $A_V^{\text{counts}} = 1$. The higher the degree of non-uniformity of the cloud, the flatter the shape of the counts-based effective extinction curve; the limiting shape (for $A_V^{\text{sheet}}/A_V^{\text{counts}} = 0$) is determined only by the relative values of the $UBVRI$ star count slopes S_{lambda} .

Fig. 13.— Comparison of A_V estimates derived using various methods (left to right): scaled from $100\mu\text{m}$ brightness and far infrared color temperature measurements (Sec. 3), cumulative star counts in the $UBVRI$ bands (Sec. 4), cumulative color distributions (Sec. 5.1), and UBV and BVI color-color diagrams (Sec. 5.2). Most error bars do not exceed the symbol sizes, and, for the sake of clarity, have not been plotted. There is good agreement amongst the different A_V estimates. The dotted line in panel 1 (RCrA “on2”) shows A_V values for a two-phase clumpy dust model (Sec. 6.2; Fig. 12) in which a fraction $(1 - f) = 0.2$ of the area is covered by optically-thick clumps; the range of $A_V^{100\mu\text{m}}$ values (IR) indicated corresponds to $A_V = 2.4 - 3.5$ mag in these dense clumps. Open symbols indicate A_V estimates based on the standard $R_V = 3.1$ interstellar extinction law; filled symbols are based on a non-standard extinction law ($R_V = 1.7$) which appears to be favored by the color excess data in all fields. For Paley 1 and Paley 3, only the “on2” estimates are reliable and these are plotted.

This figure "figure1.jpg" is available in "jpg" format from:

<http://arxiv.org/ps/astro-ph/9901422v1>

This figure "figure2.gif" is available in "gif" format from:

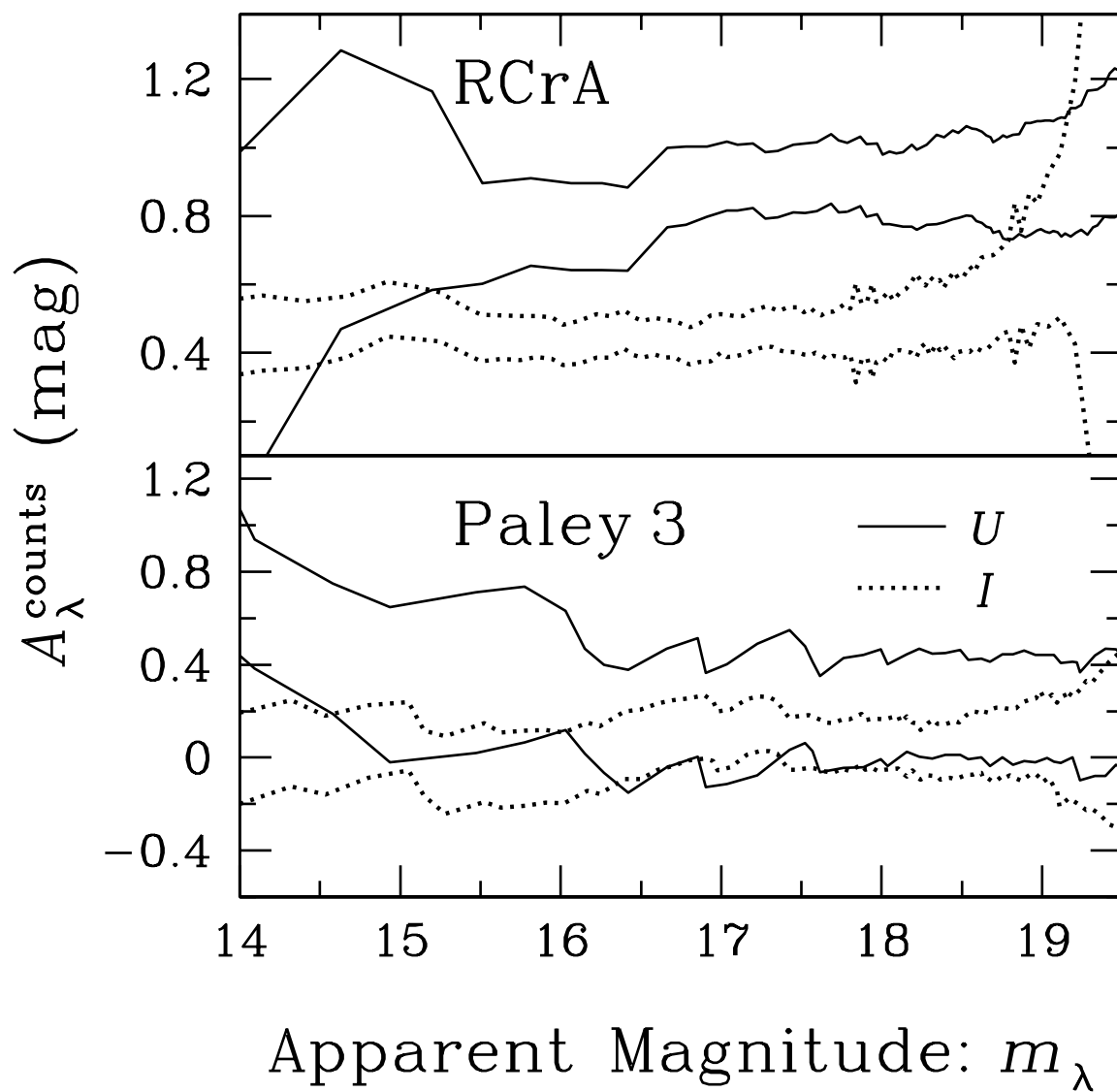
<http://arxiv.org/ps/astro-ph/9901422v1>

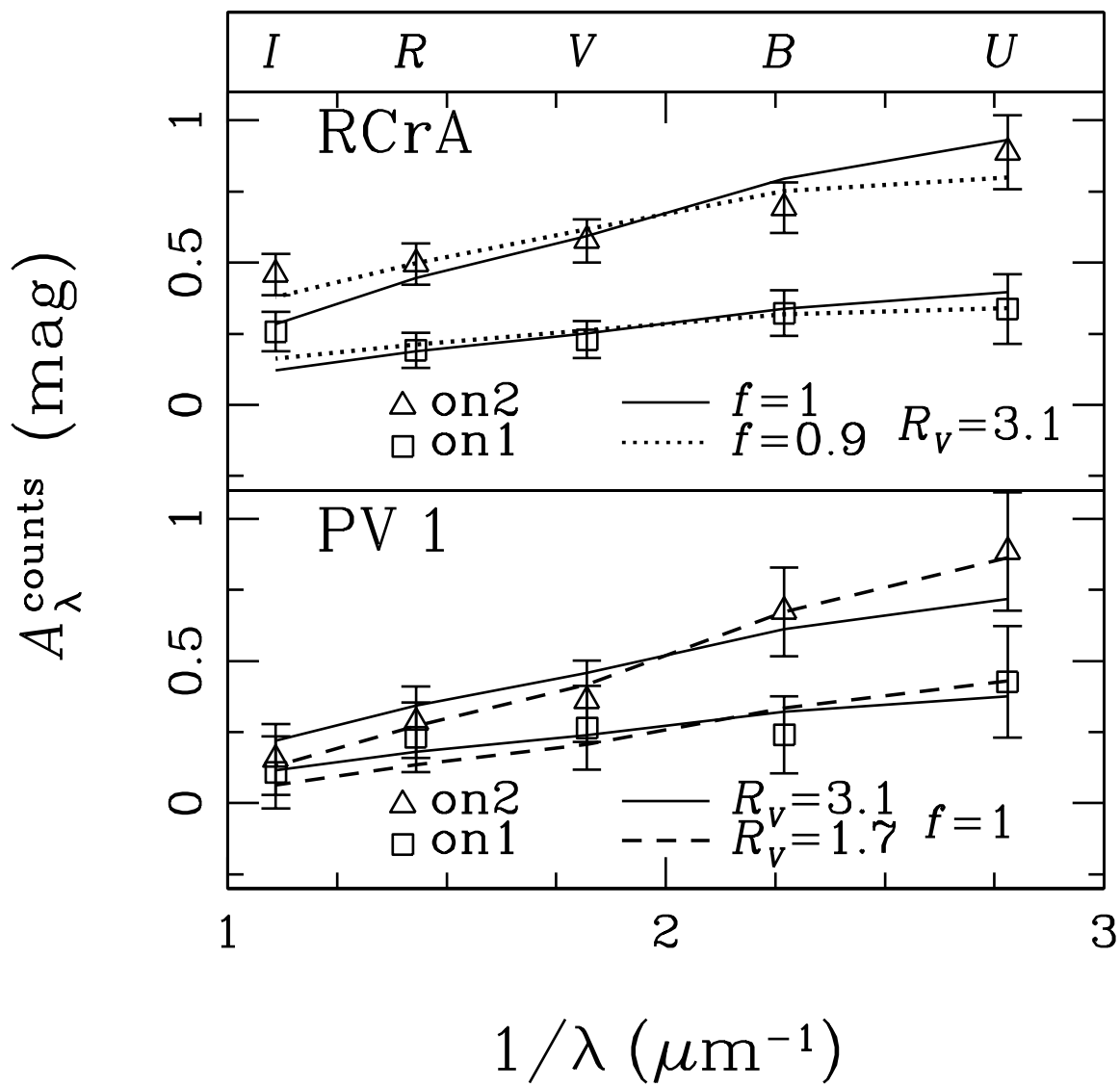
This figure "figure3.gif" is available in "gif" format from:

<http://arxiv.org/ps/astro-ph/9901422v1>

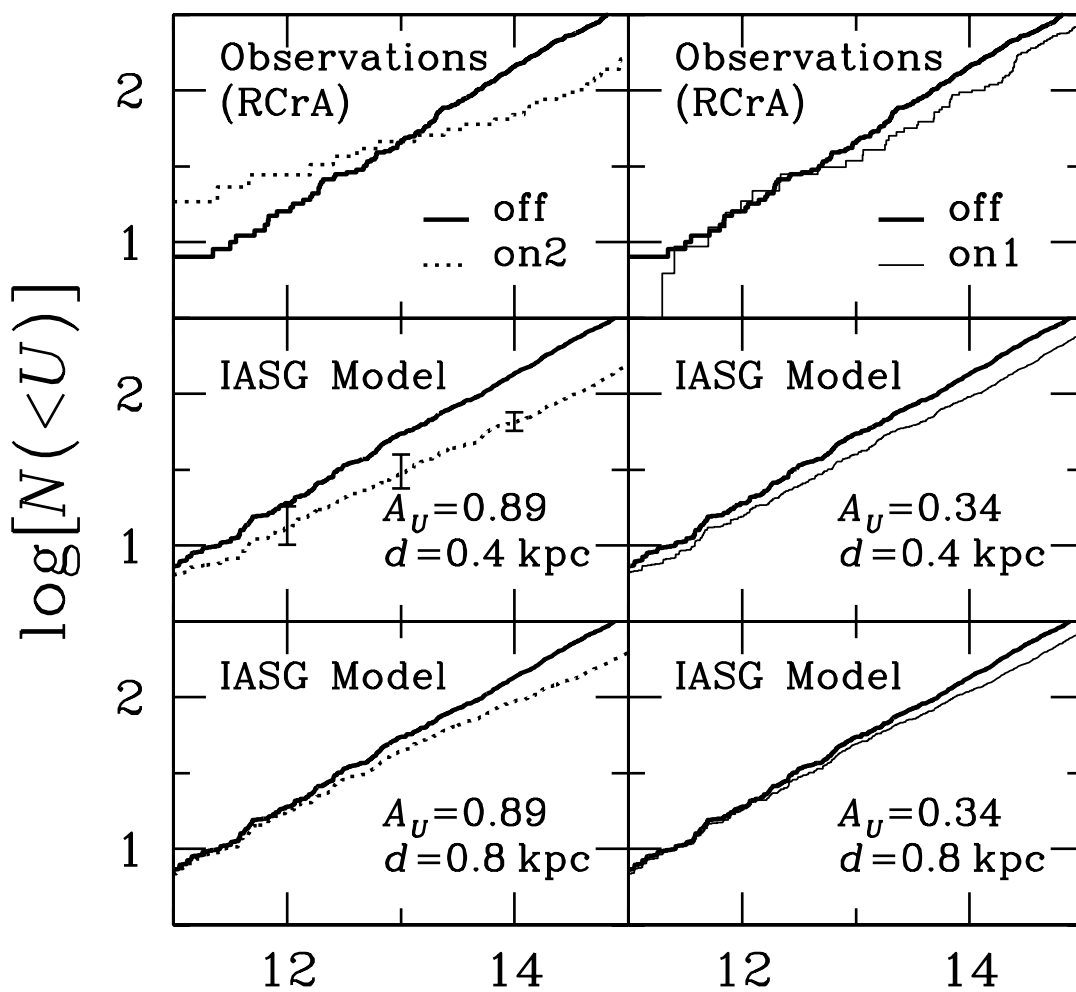
This figure "figure4.gif" is available in "gif" format from:

<http://arxiv.org/ps/astro-ph/9901422v1>



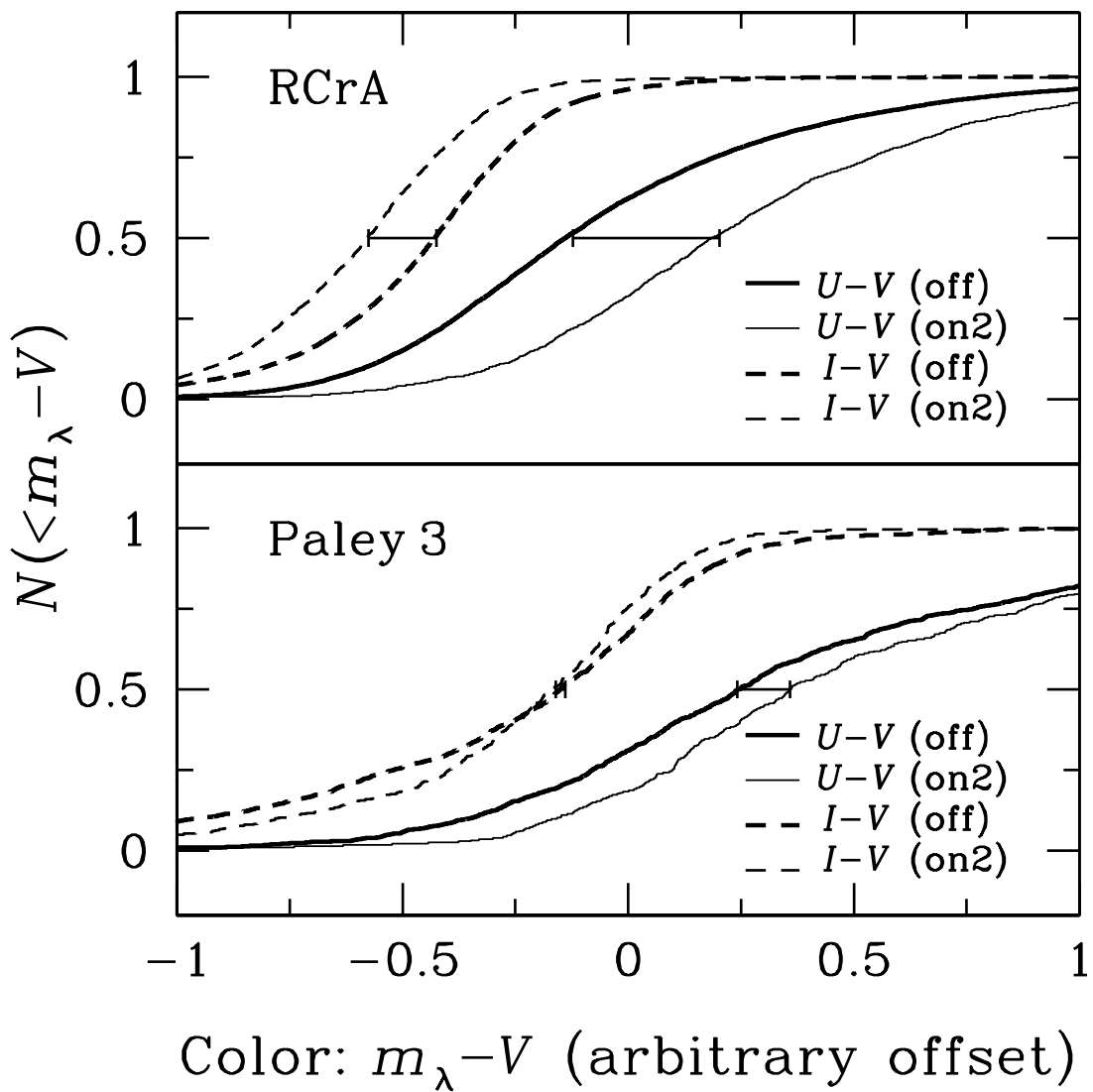


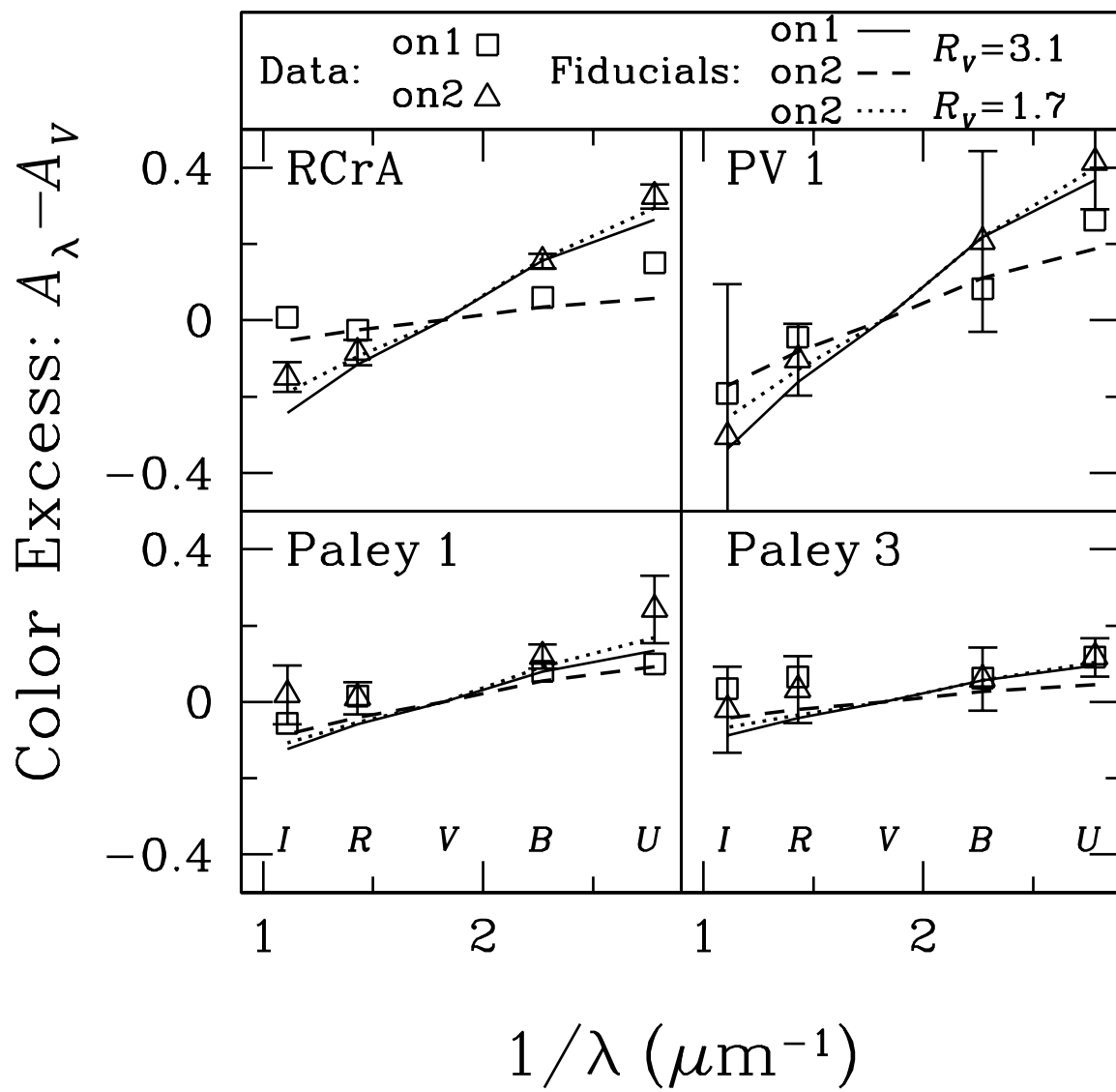
Cumulative Star Counts:



Apparent Magnitude: U

Cumulative Color Distribution:





This figure "figure10.gif" is available in "gif" format from:

<http://arxiv.org/ps/astro-ph/9901422v1>

